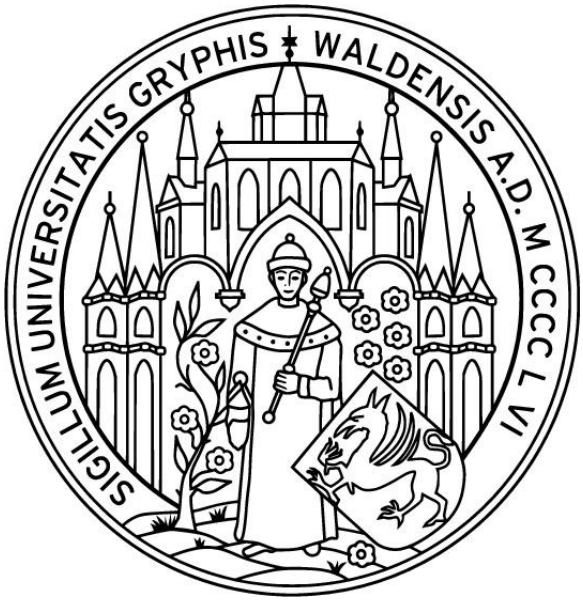

Mathematisch-Naturwissenschaftliche Fakultät
Ernst-Moritz-Arndt-Universität Greifswald

Masterarbeit

Kinetic modelling of complex plasmas

Tim Teichmann
Greifswald, den 26. August 2012

Gutachter:
Prof. Dr. Ralf Schneider
Prof. Dr. André Melzer

Contents

1 Introduction

Plasmas are ionized gases containing ions and electrons. They occur naturally in lightnings in the atmosphere [1], northern light in the ionosphere [2], the sun [3], the rings of Saturn [4], etc.. They are also used in a wide variety of technical applications ranging from fluorescent lamps [5] and plasma displays [6] to material processing [7], electronic engineering [8] and nuclear fusion experiments [9].
Even the simplest plasmas, consisting just of electrons and one ion species, show complex behaviour like drifts or waves. Plasmas can become even more complex, when additional species are introduced, chemical reactions occur or wall effects become important. This thesis deals with complex plasmas, because a second negative species is existing in addition to the electrons. In the first part this species are negative Oxygen ions. They are as immobile as positive ions, but react to electric fields inside the plasma with forces in opposite direction. Adding an additional species also increases the number of reaction channels introducing further complexity and instabilities. In the second part plasmas containing a dust grain are studied. The large dust particle can collect a very large electric charge, which modifies strongly the physics in its proximity.

Simulations of physical systems are often helpful, because they allow to study processes that are hard to be seen by experiments, because measurements are often averaged over larger areas or methods are invasive. Kinetic modelling, as it is done by the codes used within this thesis, allows to simulate plasmas with minimal assumptions. Because particles with properties as in a real plasma are simulated self-consistently, it is possible to implement virtual diagnostics into such codes, that model those used in an experiment.

The topic of the thesis is the study of those two types of complex plasmas using kinetic simulations. The use of computational physics besides experimental and theoretical physics allows the direct comparison of theoretical concepts, implemented as numerical algorithms on the computer, for realistic systems. In the first part of the thesis, a direct simulation and analysis of an experiment is presented, introducing a virtual diagnostics of electron detachment in electronegative Oxygen plasmas and comparing the results with experiment. This analysis gives a better insight into the processes determining the experimental observations. Computa-

tional physics allows also to quantify differences between different theoretical and numerical approaches for complex systems. The second part of the thesis deals with benchmarking of two different kinetic approaches to simulate dusty plasmas. Here, the comparison of results obtained with two different codes which have different numerical methods and physics assumptions allows again a better understanding of the system.

After introducing some basic physics the concepts of the codes used in this thesis are discussed. The first example for the effects of introducing additional species into a simple electron and single ion species plasma is the simulation of electronegative Oxygen plasmas, where negative Oxygen ions are formed. Here, particular emphasis is on the analysis of an experiment by Küllig et al. [10], where photodetachment was used for measuring the densities of negative Oxygen ions with a non-invasive technique. A virtual diagnostics is introduced into the code to treat the photodetachment process of negative ions within a diagnostic volume and the dynamics of this additional source of electrons in the bulk of an Oxygen plasma is analysed in detail. Particularly, the relaxation process is studied and compared with the experimental results. Afterwards, a second type of complex plasmas is studied, namely plasmas with additional dust particles. These dusty plasmas are used for benchmarks of codes using different approaches. Results from a fully self-consistent P3M code by Konstantin Matyash [11] are compared to results from Ian Hutchinson's code SCEPTIC [12]. This comparison also allows better understanding of the fundamental physics of such plasmas. Finally, the results are summarized.

2 Basic physics and methods

2.1 Basis plasma properties

A plasma is a partially ionized gas. All charged particles follow Maxwell's equationsi, but when there are no magnetic fields or currents large enough to induce them, which is the case in most low-temperature plasmas, all but Gauss' law $\nabla \cdot \mathbf{E} = \frac{\rho}{\varepsilon_0}$ can be omitted. From the definition of the electric field $\mathbf{E} = -\nabla\Phi$ one gets Poisson's equation

$$-\Delta\Phi = \frac{\rho}{\varepsilon_0}$$

which is the fundamental equation of electrostatics.

2.1.1 Boltzmann relation

In the equilibrium the forces exerted on a particle from gas pressure and the electric field must be equal. Using the ideal gas law allows to find an expression for the relation between the potential and the density n_s of a species with charge q_s [7].

$$\begin{aligned} 0 &= q_\mathrm{s} n_\mathrm{s} \mathbf{E} + \nabla p_\mathrm{s} \\ &= -q_\mathrm{s} n_\mathrm{s} \nabla\Phi + \mathrm{k_B} T_\mathrm{s} \nabla n_\mathrm{s} \\ &= \nabla (q_\mathrm{s}\Phi - \mathrm{k_B} T_\mathrm{s} \ln n_\mathrm{s}) \end{aligned}$$

Integrating and rearranging leads to Boltzmann's equation

$$n_\mathrm{s} = n_{\mathrm{s},0} \cdot \mathrm{e}^{-\frac{q_\mathrm{s}\Phi}{\mathrm{k_B} T_\mathrm{s}}}$$

with the species density in a quasi-neutral region $n_{\mathrm{s},0} = n_\mathrm{s}(\Phi = 0)$.

2.1.2 Debye length

When an object with charge Q is added to the plasma, particles of opposite charge will move towards it, while particles of the same charge will get pushed away. All in all the charge density around the object changes such to shield it. The length scale at which this happens is called Debye length. Because electrons are the most mobile species, the electron Debye length is usually very the smallest scale determining the total Debye length. It can be derived by substituting the (linearized) Boltzmann

relation in Poisson's equation [7, 13]. Ions are assumed to be singly charged and stationary, i.e. they are assumed to not react to the perturbation $n_\mathrm{i} = n_{\mathrm{e},\infty} = n_0$.

$$\begin{aligned}
\Delta\Phi &= -\frac{\mathrm{e}}{\varepsilon_0}\cdot\left(\frac{Q}{\mathrm{e}}\cdot\delta(r) + n_\mathrm{i} - n_\mathrm{e}\right) \\
&= -\frac{n_0\mathrm{e}}{\varepsilon_0}\cdot\left(1 - \cdot\mathrm{e}^{\frac{e\Phi}{\mathrm{k_B}T_\mathrm{e}}}\right) + \frac{Q}{\varepsilon_0}\cdot\delta(r) \\
&= -\frac{n_0\mathrm{e}}{\varepsilon_0}\cdot\left(1 - \cdot\left[1 + \frac{e\Phi}{\mathrm{k_B}T_\mathrm{e}}\right]\right) + \frac{Q}{\varepsilon_0}\cdot\delta(r) \\
\Delta\Phi &= \frac{n_0\mathrm{e}^2\Phi}{\mathrm{k_B}T_\mathrm{e}} + \frac{Q}{\varepsilon_0}\cdot\delta(r)
\end{aligned}$$

If the potential around the object is assumed to be spherically symmetric, one can solve the differential equation with

$$\Phi = \frac{Q}{4\pi\varepsilon_0 r}\cdot\mathrm{e}^{-\frac{r}{\lambda_\mathrm{De}}}$$

where

$$\lambda_\mathrm{De} = \sqrt{\frac{\varepsilon_0\mathrm{k_B}T_\mathrm{e}}{\mathrm{e}^2 n_0}}$$

is the electron Debye length. The solution itself is referred to as Debye-Hückel or Yukawa potential.

2.1.3 Plasma frequency

The shortest timescale in non-magnetized plasmas is determined by plasma oscillations of electrons. They occur when all electrons in a volume element are displaced by a certain distance x. The force equation delivers [7]

$$\begin{aligned}
m\ddot{\mathbf{x}} &= -\mathrm{e}\mathbf{E} = -\mathrm{e}\frac{e n_0 \mathbf{x}}{\varepsilon_0} \\
&= -\frac{\mathrm{e}^2 n_0}{\varepsilon_0 m}\cdot\mathbf{x}
\end{aligned}$$

which defines the electron plasma frequency:

$$\omega_\mathrm{pe} = \sqrt{-\frac{\mathrm{e}^2 n_0}{\varepsilon_0 m}}$$

Whenever one models a physical system, effects have to be resolved temporal and spatially. In typical low-temperature plasmas the shortest length and time scales are Debye length and plasma frequency.

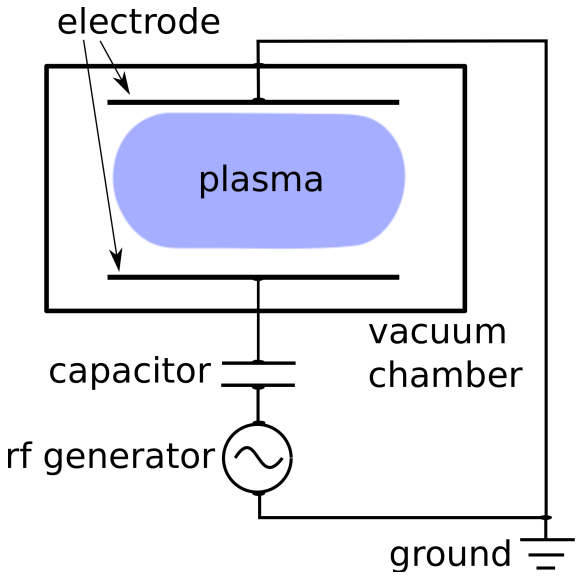

Fig. 2.1: Scheme of a typical ccrf plasma chamber [14].

2.2 RF plasmas

A widely used mechanism for sustaining low-temperature plasmas is the so-called capacitively coupled radio frequency (ccrf) heating. Two electrodes, usually parallel plates, are built into a vacuum chamber filled with a gas. A sketch of this is given in figure 2.1. At one of these electrodes an oscillating voltage is applied. The frequency is usually 13.56 MHz. Only electrons are mobile enough to follow the quickly varying rf field. This makes their velocity distribution functions highly time-dependent and non-Maxwellian. The latter is also true for ions, when mean free paths are long against the plasma dimensions [14]. Even though ccrf discharges are widely used, their underlying processes are not yet fully understood. The non-Maxwellian characteristics make an analytical approach very hard. More in-depth descriptions can be found for example in [7].
Rf generated plasmas consist of a bulk region with near constant potentials and densities, and a sheath region in which the potential drops to the one of the electrode built up by the much faster moving electrons. The field in this region accelerates ions and decelerates electrons coming from the bulk guaranteeing total current balance of both species. This leads to an overall positive charge density close to the wall on the length-scale, where charge separation in plasmas is possible. Therefore, the so-called sheath establishs in the order of several Debye lengths. Because electron velocities change during the rf cycle, the amount of electrons in the sheath, and therefore the charge density, oscillates. On average electrons gain energy when they are repelled by this “moving” sheath. This “stochastic heating” at low densi-

ties produces electrons with higher energies, resulting in a typical Bi-Maxwellian distribution function with cold bulk ions and a hot tail.. The region between bulk and sheath is called pre-sheath. Quasineutrality is still guaranteed there, but the potential is already decreasing.

2.3 Electronegative plasmas

The creation of negatively charged ions in a plasma, like Oxygen, raises its complexity. More species lead to more possible reaction channels, which makes the equilibrium densities more dependent on the local temperatures and densities of all species. The ratio between negatively charged ion and electron density is called electronegativity:

$$\alpha = \frac{n_-}{n_\mathrm{e}}$$

At high electronegativities, plasma dynamics can be changed. When there are only few electrons in a plasma charge transport becomes slower and the Debye length increases. This interdependences can allow small changes in the system to drive complex processes until equilibrium is restored.

2.4 Dusty plasmas

If a low-temperature plasma does not only contain electrons, ions and neutrals, but also particles of micron or sub-micron size it is referred to as a “dusty” plasma [15]. In contrast to plasma particles at the molecular scale, dust particles do not have constant charge. Instead they get charged by absorbing plasma electrons and ions. A newly immersed dust grain will first be hit by electrons, because they are much more mobile. The dust will therefore become negatively charged. This will repel further electrons and attract (positive) ions. After some time the ion and electron fluxes balance. The charge will then fluctuate around a constant average value. This way they can collect $10^3 \ldots 10^5$ elementary charges, which allows them to heavily influence the plasma particles near them. Their large size and therefore mass of about $3 \cdot 10^{11}$ proton masses makes them very immobile [13].

A classical approach to analytically find the potential of dust grains is the Orbital Motion Limit (OML) theory. It was originally developed to explain the voltages measured with Langmuir probes [16, 17]. For this theory it is assumed that the dust already has a potential Φ_d and particles with mass m and charge q start from infinity with a Maxwellian velocity distribution. The main idea is to calculate an effective cross section of the dust via energy and angular momentum conservation. Typical particle trajectories can be seen in figure 2.2.

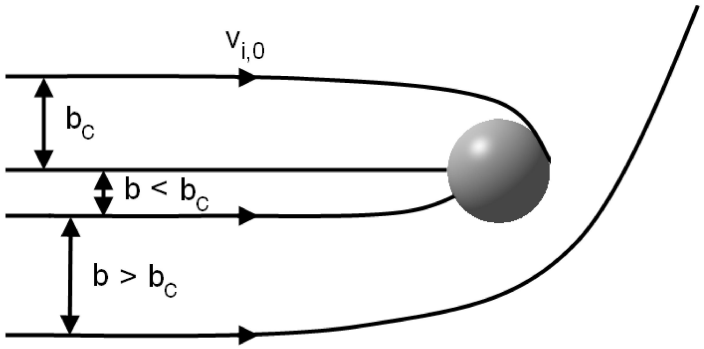

Fig. 2.2: Representative particle orbits near a dust grain as described by OML [14].

For the derivation given here [13] the axis is set parallel to the particles initial velocity v_0 and passes through the dust center. Polar coordinates (r,θ) are used near the dust. The initial distance between particle and axis is called "impact parameter" b. Energy and angular momentum conservation

$$\begin{array}{lllll} W_0 & = & \frac{m}{2}v_0^2 & = & \frac{m}{2}\left(v_r^2 + r^2\dot{\theta}^2\right) + q\Phi \\ J_0 & = & mv_0 b & = & mr^2\dot{\theta} \end{array}$$

can be combined to find an expression for the impact parameter.

$$b = r \cdot \sqrt{1 - \frac{q\Phi(r)}{W_0} - \frac{mv_r^2}{2W_0}}$$

All particles with an impact parameter below b_c hit the dust, all others pass. The critical impact parameter is the one at which particles reach the dust radius $r = R_\mathrm{d}$ without radial velocity:

$$b_\mathrm{c} = r_\mathrm{d} \cdot \sqrt{1 - \frac{q\Phi_\mathrm{d}}{W_0}}$$

The effective collection cross section changed from πr_d^2 to πb_c^2. With this cross section one can calculate the current

$$I_\mathrm{s} = q \int_{v_0}^{\infty} 4\pi b_\mathrm{c}^2(v) \cdot v \cdot f(v)\,\mathrm{d}v$$

by integrating over the charge flux over all velocities, that can reach the probe. $v_0 = (2q\Phi/m)^{1/2}$ is the velocity needed to overcome a repulsing potential or the maximum velocity that a particle can have in the opposite direction and still be absorbed. This leads to the positive and negative fluxes:

$$\begin{aligned} I_- &= qn\pi r_\mathrm{d}^2 \left(\frac{m}{2\pi \mathrm{k_B} T_-}\right)^{3/2} \int_{v_0}^{\infty} 4\pi v \left(v^2 - v_0^2\right) \exp\left(-\frac{mv^2}{2\mathrm{k_B}T}\right) \mathrm{d}v \\ &= qn\pi r_\mathrm{d}^2 \left(\frac{\mathrm{k_B} T_-}{2\pi m}\right)^{1/2} \exp\left(-\frac{q\Phi}{\mathrm{k_B}T}\right) \\ I_+ &= qn\pi r_\mathrm{d}^2 \left(\frac{m}{2\pi \mathrm{k_B} T_+}\right)^{3/2} \int_{-v_0}^{\infty} 4\pi v \left(v^2 + v_0^2\right) \exp\left(-\frac{mv^2}{2\mathrm{k_B}T}\right) \mathrm{d}v \\ &= qn\pi r_\mathrm{d}^2 \left(\frac{\mathrm{k_B} T_+}{2\pi m}\right)^{1/2} \left[1 - \frac{q\Phi}{\mathrm{k_B}T}\right] \end{aligned}$$

Because the dust is not connected to any conducting objects, the positive and negative currents must compensate:

$$\mathrm{e}n_\mathrm{e} \left(\frac{\mathrm{k_B} T_\mathrm{e}}{2\pi m_\mathrm{e}}\right)^{1/2} \exp\left(-\frac{q\Phi}{\mathrm{k_B}T_\mathrm{e}}\right) = I_\mathrm{e} = I_\mathrm{i} = qn_\mathrm{i} \left(\frac{\mathrm{k_B} T_\mathrm{i}}{2\pi m_\mathrm{i}}\right)^{1/2} \left[1 - \frac{q\Phi}{\mathrm{k_B}T_\mathrm{i}}\right]$$

This is the OML equation for the floating potential of a dust grain. It can only be solved numerically.

2.5 The Particle-In-Cell method

Even low density plasmas, e.g. glow discharges, consist of billions of charged particles per cubic centimetre [13]. This number is usually way too high to trace them all in a computer simulation. Depending on which aspect of the plasma one is interested in, the computational effort can be reduced by scaling down the system size, treating the different species as fluids or by grouping many particles with close positions and velocities (and of the same species) into so called “super particles”. On the following pages it is assumed, that the latter approach is chosen.

Each of the super particles has a position in space and a velocity, which represents the mean value of the original particle’s respective properties. Since the charge-to-mass ratio does not change when combining particles to such super-particles, electromagnetic forces induce the same motion as they would on the real particles. This means super particles can be interpreted as a sample of particles in the plasma. It can be proven that for collisionless plasmas the solutions obatined wih such super-particles are identical to the solution of the Vlasov equation for real particles [18].

The most straight forward approach for applying dynamics would be calculating and applying the forces, that each pair of particles exerts on one another. Such Particle-Particle (PP) models do however scale very bad for large particle numbers, since $\frac{N(N-1)}{2}$ forces must be calculated and applied for N super particles in the system. While the calculation of short range forces can be accelerated by considering only interactions between very close particles, this is not possible for long range interactions like electrostatic forces.

To cope with this problem the so-called "Particle-In-Cell" method was introduced [18, 19]. It utilizes the fact that small deviations of a particle's position have only minor influence some distance away. Its main idea is to use a grid overlaying the simulated area for solving the Poisson's equation instead of calculating the forces from PP models. All super particle charges are interpolated and summed up to charge densities on the points of this grid. Poisson's equation can then be solved on the grid, the fields are then interpolated back to the particles to accelerate them. This way the number of calculations per timestep grows only linearly with the number of super particles (or grid points) instead of quadratic dependence. One should note, that solving Poisson's equation is only sufficient when currents in the plasma are low. At higher currents all of Maxwell's equations must be considered, which requires calculation of the current and makes force calculations much more complicated.

For reasons of simplicity super particles are referred to as particles in this thesis.

3 Numerical implementation

Three different codes have been used for the simulations. All of them are based on the Particle-In-Cell method.

3.1 The 1D3V-PIC

The model I used to simulate Oxygen plasmas is a PIC code with Monte Carlo collisions written by Konstantin Matyasah [11, 20].

3.1.1 Particles

The species considered for the simulation are e, O_2^+, O^-, O and O_2. Each simulated super particle represents a fixed number of particles of one of those species. The equations of motion for plasma particles are only determined by the charge to mass ratio. Therefore, these super particles obey the same dynamical equations and guarantee, even mathematically exact, the same kinetic solutions as following the individual particles [18]. Correct inclusion of collisions using Monte Carlo methods requires the resolution of all three Cartesian components of the velocity. The discharge analysis is done just along the axis. Therefore, the spatial complexity of the simulation is reduced to one dimension and only this component is stored for all the particles. .
All super particles except O_2 neutrals represent the same number of particles (or density) in a real system. Because there are much more neutrals than charged particles in a weakly ionized plasma, neutral super particles represent a much larger number of particles. Furthermore, up to 100 of them are grouped into "super-super" neutrals with same position and velocity to increase their statistical weight without increasing computational costs [11].

3.1.2 Units

To avoid numerical instabilities in a PIC simulation the smallest relevant temporal and spatial scales must be resolved. In the case of weakly collisional plasmas these are usually Debye length λ_{Db} and plasma frequency ω_{p}^{-1} [21]. To transform the equations into a dimensionless form, a reference electron density n_0 is defined and the resulting electron Debye length λ_{De} and plasma frequency ω_{pe} are calculated.

The cell width is set to be $\Delta x = 0.5\,\lambda_{\mathrm{De}}$ and timesteps are $\Delta t = 0.2\,\omega_{\mathrm{pe}}^{-1}$ guaranteeing numerical stability [11]. All other values are normalized to this length and this time.
The number of super particles N_{D} in a cube of the volume λ_{De}^3 (or in 1D a section of length λ_{De}) represents the reference density of n_0.

3.1.3 Simulated region

The simulated region is divided into an equidistant mesh. Cells can be interpreted as indefinitely expanded slices of the plasma, with all parameters being constant within them. This approximation is valid as long as gradients perpendicular to the resolved direction are very small. This holds true at least in the area close to the axis. In this code, transport effects can only be simulated in the resolved spatial direction, namely along the axis. The model can only calculate realistic results if transport is negligible in all other directions.
On both ends of the calculation domain electrodes need to be implemented. The left one always is chosen as grounded with a potential of 0 V. The right electrode's potential harmonically oscillates around 0 V at a frequency of 13.56 MHz. The amplitude is used as a system parameter and not calculated from the heating power applied in experiments and the electrical network outside the plasma. This approach allows direct analysis of trends and avoids the need for the solution of an additional differential equation.

3.1.4 Field calculation

The relevant quantity for the Poisson equation is the charge density, which needs to be calculated on the grid. Just counting the charges in one cell without using a shape function introduces too large amount of noise, because small positional changes of particles close to cell boarders can lead to strong fluctuations in charge density. A much better approach is to consider the charge of all particles to be blurred. The charge density is largest at their position and decreases linearly in space until it reaches zero one cell half cell width away. This applies in all directions along the grid (i.e. the charge distribution would look like a pyramid in 2D). The neighbouring grid points "collect" charges in an area as large as one cell, so the charge mapped to a grid point looks like a pyramid again (but with the doubled side length). One can show that the sum of charges mapped to all grid points by a particle conserves the charge of the particle [21]. By summing up the results of this interpolation over all particles a charge density can be calculated on the grid.
This discrete charge density is calculated every timestep. Poisson's equation

$$\nabla^2 \Phi = -\frac{\rho}{\varepsilon_0}$$

is discretized by using potentials Φ_i on the grid points, finite differences for the Laplace operator and the charge densities ρ_i, which have been described above.

$$\frac{\Phi_{i+1} - 2\Phi_i + \Phi i - 1}{\Delta x^2} = -\frac{\rho_i}{\varepsilon_0}$$

For the outermost grid points the externally defined plate potentials φ are applied. The resulting tridiagonal matrix

$$\begin{pmatrix} 1 & 0 & 0 & 0 & \cdots & 0 & 0 \\ 1 & -2 & 1 & 0 & \cdots & 0 & 0 \\ 0 & 1 & -2 & 1 & \cdots & & 0 \\ \vdots & & \ddots & \ddots & \ddots & & \\ & & & & & & \\ 0 & & & & 1 & -2 & 1 \\ 0 & 0 & \cdots & & 0 & 0 & 1 \end{pmatrix} \cdot \begin{pmatrix} \Phi_1 \\ \Phi_2 \\ \\ \vdots \\ \\ \Phi_{N-1} \\ \Phi_N \end{pmatrix} = \frac{(\Delta x)^2}{\varepsilon_0} \begin{pmatrix} \varphi_1 \\ \rho_2 \\ \\ \vdots \\ \\ \rho_{N-1} \\ \varphi_N \end{pmatrix}$$

is solved with forward and backward substitution substitution as described e.g. in [22].

3.1.5 Particle motion

In every timestep all electrons are accelerated

$$\mathbf{v} = \mathbf{v}_{\text{old}} + \mathbf{v} \cdot \Delta t$$

and then moved with their new velocity

$$\mathbf{x} = \mathbf{x}_{\text{old}} + \frac{q}{m}\mathbf{E} \cdot \Delta t$$

Where $\mathbf{E}$ is the electric field interpolated from the field at the grid points. This is done using the same equation as for interpolating charges to the grid points guaranteeing by this momentum conservation [21]. If particles reach the domain borders, they are removed and may produce secondary electrons on impact.
The same mechanism is also applied to ions and neutrals. Since they move much slower one can use sub-cycling: they are pushed only every 5 steps.

3.1.6 Collisions

Particle collisions and reactions are handled by a binary Monte-Carlo collision model, as used by Takizuka and Abe [21, 23] for Coulomb collisions.

For every implemented reaction type, all particles in one cell are randomly grouped into pairs with one particle of each reactant species in them. For each of these pairs the relative velocity v_{rel} is calculated. The reaction probability can then be determined using the equation

$$P_{\mathrm{coll}} = 1 - \exp -n \cdot v_{\mathrm{rel}} \cdot \sigma \cdot \Delta$$

with the velocity-dependent cross section σ, the timestep Δt and the density of the more abundant reactant n. Whether the collision happens or not is decided based on random numbers. If the random number is larger than the normalized collison or reaction probability the collision is not done, if it is smaller it will occur. In a collision the particles' velocities are split into a relative and a center-of-mass component. In case of inelastic collisions or reactions the energy in the relative motion is adjusted according to the losses. If the collision is a reaction reactants are destroyed and products are created at the location of the removed particle. Finally, the direction of relative motion is changed randomly and the relative energy is distributed to the particles again according to momentum and energy conservation.

In addition to normal collisions the following reactions are implemented in the code:

O_2	+	e	$\longrightarrow$	O	+	O^-			dissociative attachment
O_2	+	e	$\longrightarrow$	O_2^+	+	2e			electron impact ionization
O^-	+	O_2	$\longrightarrow$	O	+	e	+	O_2	detachment on neutrals
O^-	+	O_2^+	$\longrightarrow$	O_2	+	O			mutual neutralization
O_2^+	+	e	$\longrightarrow$	O	+	O			dissoziative recombination
O^-	+	e	$\longrightarrow$	O	+	2e			electron impact detachment

Investigations with a 0D model [24] showed, that these are the most relevant processes in the parameter ranges of the plasmas considered here. One should note, that excited particles are not tracked as separate species but determined from ground state populations. For the plasmas studied here higher charged ions like O_2^- and O_3 can also be neglected.

3.2 The P3M-PIC

The Particle-Particle Particle-Mesh (P3M) code used to self-consistently model the plasma with a dust grain is another variant of the 1D3V-PIC described in section 3.1. It was also written by Konstantin Matyash and has been modified by Ramana Ikkurthi [25] and Lars Lewerentz [14]. The most notable differences from the 1D3V code already presented are:

- The simulated area is three-dimensional. This means, the particles' position holds all three components. Cells are now cubes instead of sections on a line. Field calculations, density and force interpolations have to be performed three-dimensional, which is described below.

- The system is periodic in x and z direction. Particles leaving the domain have their position adjusted accordingly.

- The electrodes are placed at the ends of the system in y-direction. The time-dependent RF-voltage is applied there. Particles hitting the electrodes are removed, but might emit secondary electrons.

- An Argon plasma is simulated. Condsidered species are Ar, Ar^+ and e (where super-super particles are used for Ar). Besides several collisions and excitations the only implemented reaction is electron impact ionization.

- To reduce the runtime parallelization is used. To achieve this, the domain is decomposed into sub-domains along the y axis. This allows parallel processing of these domains by multiple processors.

- The possibility to add a dust particle was introduced. More on the implications of this will be given below.

3.2.1 Field calculation

The discretized Poisson's equation on a three-dimensional grid is given by

$$\frac{\Phi_{i+1,j,k} + \Phi_{i-1,j,k} + \Phi_{i,j+1,k} + \Phi_{i,j-1,k} + \Phi_{i,j,k+1} + \Phi_{i,j,k-1} - 6\Phi_{i,j,k}}{\Delta x^2} = -\frac{\rho_{i,j,k}}{\varepsilon_0}$$

which transforms into a seven band matrix. Solving this system with forward and backward iteration is still very efficient, but since the algorithm relies on triangular matrices, the discretized Laplace operator must be LU decomposed [22]. This means two matrices L and U must be found, such that

$$\begin{pmatrix} l_{11} & 0 & 0 & \cdots & 0 \\ l_{21} & l_{22} & 0 & \cdots & 0 \\ l_{31} & l_{32} & l_{33} & \ddots & \vdots \\ \vdots & \vdots & \ddots & \ddots & 0 \\ l_{n1} & l_{n2} & l_{n3} & \cdots & l_{nn} \end{pmatrix} \cdot \begin{pmatrix} u_{11} & u_{12} & u_{13} & \cdots & u_{1n} \\ 0 & u_{22} & u_{23} & \cdots & u_{2n} \\ 0 & 0 & u_{33} & \cdots & u_{3n} \\ \vdots & \vdots & \ddots & \ddots & \vdots \\ 0 & 0 & 0 & \cdots & u_{nn} \end{pmatrix}$$

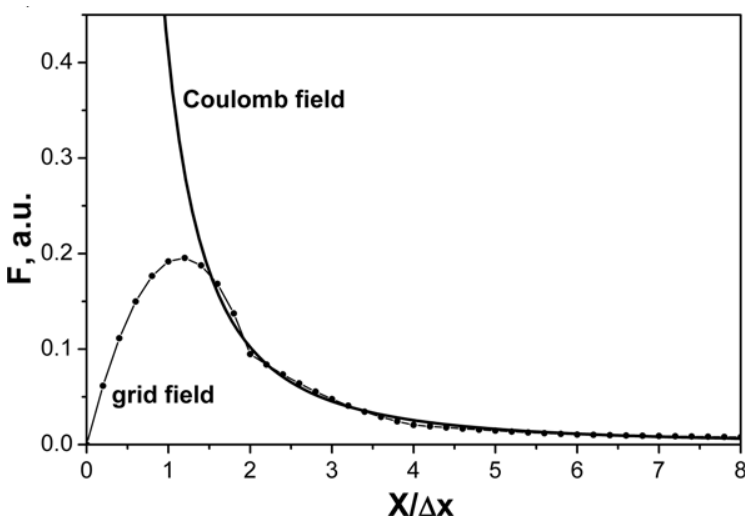

Fig. 3.1: Comparison of the force between two charged particles that interact directly or by mapping their charges onto a grid first [26].

equals the matrix representation of the Laplace operator. This is done using the SuperLU library. Because the Laplace operator is represented by a constant matrix determined only by the geometry of the mesh, it is sufficient to perform the numerically expensive decomposition just once in the initialization phase of the code. Only the fast forward and backward solver has to be used in every timestep.

3.2.2 Field calculation near the dust

As soon as the background plasma equilibrates an initially uncharged, spherical dust grain can be added to the plasma. It can change its charge by absorbing other particles. For most of the simulated domain such a dust grain is treated like any other particle for the charge density and potential calculation within the regular PIC approach.

It is a well-known drawback of PIC simulations, that it strongly diminishes near-range interactions [21]. This is an effect of mapping the charges to the mesh. Because a particle must not exert forces on themselves, the force between two particles within the same cell decreases when they come closer. In a real system the Coulomb force would grow larger instead. This is illustrated in figure 3.1. Because accurate orbits near the dust are essential for finding out which particles get absorbed and because the dust's very high charge dominates particle motion in its proximity, the electric field must be calculated more carefully in this region.

To achieve this in a self-consistent way, the electric field contributions from the dust $\mathbf{E}_{\text{dust}}$ and from all other particles $\mathbf{E}_{\text{grid}}$ are calculated separately [27]. The acceleration of most particles is calculated as usual with $\mathbf{E} = \mathbf{E}_{\text{grid}} + \mathbf{E}_{\text{dust}}$. For particles within one Debye length from the dust, the electric field is calculated by only using the grid electric field for non-dust particles and substituting the dust component on the grid by Coulomb's law.

$$\mathbf{E}_{\text{near}} = \mathbf{E} - \mathbf{E}_{\text{dust}} + \frac{Z_{\text{d}}\text{e}}{4\pi\varepsilon_0} \frac{\mathbf{r} - \mathbf{r}_{\text{d}}}{|\mathbf{r} - \mathbf{r}_{\text{d}}|^3}$$

with the number of elementary charges absorbed by the dust Z_{d}. This calculation must be performed for every particle in the affected cells. Because of the direct interaction between particles and dust, one often refers to the affected region as "MD" (molecular dynamics) region.

3.2.3 Particle motion near the dust

Because it is of very high importance to know whether a particle near the dust is absorbed or not and because the Debye-Hückel potential shows a strong spatial dependency, particle motion is subcycled for all particles in the MD region and particles are pushed more often with smaller steps accordingly. As soon as a particle reaches the inside of the grain it is deleted and its charge is transfered to the dust – it is absorbed.

3.3 SCEPTIC

During the last ten years Ian H. Hutchinson and Leonardo Patacchini developed and implemented a method to simulate the effects of a spherically shaped object (e.g. a Mach probe) on a surrounding flowing plasma. The result is the SCEPTIC code, which is short for "Specialized Coordinate Electrostatic Particle and Thermals In Cell". From the basic concept it is a two dimensional Particle-in-Cell code, but it contains several differences.

3.3.1 Cells and particles

In SCEPTIC only one type of ions is considered and only ions are treated as particles. They have positions and velocities in all three Cartesian coordinates (x, y, z), where z is the direction in which ions are drifting. Other than in most PIC codes, super particles do not represent a fixed quantity of ions. Instead, their number is kept constant during the whole simulation by reinjecting every lost particle. How much real particles they represent is coupled to the densities at infinity $n_{\text{i},\infty} = n_{\text{e},\infty}$. Because velocity distributions at the boundary are known, it is possible to compare

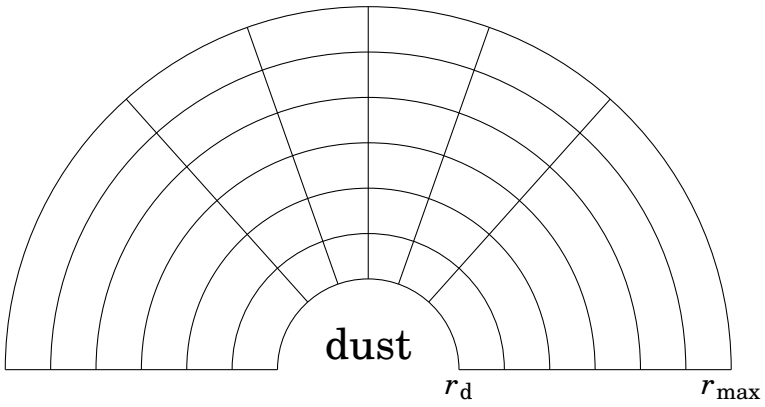

Fig. 3.2: A scheme of the grid SCEPTIC uses for potential calculations.

the real flux into the region with the number of reinjected particles. The weight of the particles is then adjusted every step. After some time the equilibrium is reached.
Electrons are considered as an infinitely quick responding background with density

$$n_{\mathrm{e},\infty} \cdot \exp\left(\frac{\mathrm{e}\Phi}{\mathrm{k_B}T_\mathrm{e}}\right)$$

determined by the Boltzmann relation [28].

Cells are only two dimensional and curvilinear instead of rectangular. They are equally sized in radius r and cosine of azimuthal angle θ [28]. Such a grid is depicted in figure 3.2. The third dimension is the polar angle φ. Because the simulated system only contains a spherical (and therefore symmetric) dust particle and plasma flowing plasma along the z-axis the whole system – and especially the potential – is symmetric along φ.
The simulated domain only has boundaries in r direction. The dust begins at $r = 1$ and the domain ends at $r = r_\mathrm{max}$.

3.3.2 Units and input

SCEPTIC scales temperatures in units of the electron temperature T_e and velocities in ion Bohm velocities $\sqrt{(k_\mathrm{B}T_\mathrm{e})/(Zm_\mathrm{i})}$. Distances are normalized to units of dust radii r_d. This means information on the dust size must be handed over indirectly by giving information on the Debye length. Even though the unit time in SCEPTIC can be calculated via $r_\mathrm{d}/\sqrt{(k_\mathrm{B}T_\mathrm{e})/(Zm_\mathrm{i})}$ timesteps are usually smaller than that.

3.3.3 Field calculation

Mapping of ion charges to charge densities onto a mesh is done with a cloud-in-cell scheme as described in section 3.1.4. To calculate the potential, Poisson's equation

$$\Delta\Phi = \frac{\rho}{\varepsilon_0} = \frac{e}{\varepsilon_0} \cdot \left(n_i - n_{\mathrm{e},\infty} \cdot \exp \frac{\mathrm{e}\Phi}{\mathrm{k_B} T_\mathrm{e}} \right)$$

must be solved. In contrast to the other simulations used within this thesis, direct calculation by discretizing the equation and inverting the Laplace operator is not possible, because electron density and therefore charge density is not known a priori. They depend on the local potential in a nonlinear way. That is why the solution must be achieved iteratively via the "successive over-relaxation" method with Chebyshev acceleration [22, 29]. The idea behind this is, that Poisson's equation is discretized and the left hand side is solved for Φ of the current cell.

$$\begin{aligned}\Phi_{i,j} = &\frac{a_{i,j+1}\Phi_{i,j+1} + a_{i,j-1}\Phi_{i,j-1} + a_{i+1,j}\Phi_{i+1,j} + a_{i-1,j}\Phi_{i-1,j}}{a_{i,j}} \\ &+ \frac{\mathrm{e}\left(n_\mathrm{i} + n_{\mathrm{e},\infty} \cdot \exp\left(\frac{\mathrm{e}\Phi}{\mathrm{k_B} T_\mathrm{e}} \right) \right)}{a_{i,j}}\end{aligned}$$

with the local ion density n_i. The coefficients are $a_{i\neq j} = 1$ and $a_{i=j} = 4$ for a rectangular grid, but on the curvilinear grid it is more complicated. Introducing a relaxation parameter $\omega \in (0,2)$ and rewriting the above equation into the form $\Phi^\mathrm{new} = (1-\omega)\cdot\Phi^\mathrm{old} + \omega \cdot \Delta\Phi$ increases convergence speed or numerical stability. One can show that it is possible to calculate the new potential at all grid points without using old values of potentials at grid points that have already been updated by clever matrix splitting, rearranging and forward iteration [22]. The resulting set of equations

$$\begin{aligned}\Delta\Phi^\mathrm{new}_{i,j} = (1-\omega)\cdot\Phi^\mathrm{old}_{i,j} + \omega \cdot \Bigg(&\frac{a_{i,j+1}\Phi^\mathrm{old}_{i,j+1}}{a_{i,j}} \\ &+ \frac{a_{i,j-1}\Phi^\mathrm{new}_{i,j-1} + a_{i+1,j}\Phi^\mathrm{old}_{i+1,j} + a_{i-1,j}\Phi^\mathrm{new}_{i-1,j}}{a_{i,j}} \\ &+ \frac{\mathrm{e}\left(n_\mathrm{i} + n_{\mathrm{e},\infty} \cdot \exp\left(\frac{\mathrm{e}\Phi^\mathrm{old}_{i,j}}{\mathrm{k_B} T_\mathrm{e}} \right) \right)}{a_{i,j}} \Bigg)\end{aligned}$$

is solved iteratively until convergence is achieved.

3.3.4 Boundary conditions

SCEPTIC offers several scenarios for boundary conditions during potential calculation. In most runs used within this thesis the potential at the outer boundary was set to be $\Phi_{\text{out}} = 0$.
For one series of runs a more sophisticated approach [29] was chosen. It allows more realistic potential distributions for spherically symmetric systems with $\Phi(r_{\text{b}}) \neq 0$. The basic idea is, to approximate the potential by correcting Debye's shielding equation with the simulated values at the outer boundary. Therefore potential and ion density on the boundary are measured. The difference between measured and expected ion density $n_{\text{i},\infty} \cdot (1 - Z\Phi T_{\text{e}}/T_{\text{i}}) - n_{\text{i}}$ is calculated and put into the shielding equation as a correction factor. This equation can then be solved using a Green's function approach. The first derivative of the solution is used as outer boundary condition.

For the inner boundary the probe potential can be externally defined by using an input parameter or set to be floating. Since this thesis aims to investigate the simulation of conducting, spherical dust in a plasma (which is also done by P3M), a conducting floating probe was chosen for my simulations. A third possibility would have been to use an insulating, floating probe.
In the latter two cases, the ion flux onto the probe is measured. Because ion and electron flux onto the floating probe must be identical, the probe potential can be calculated from OML theory. For Maxwellian electrons as used in SCEPTIC it follows [12]

$$\frac{n_{\text{e},\infty}}{4} \cdot \sqrt{\frac{8\text{k}_\text{B}T_\text{e}}{\pi m_\text{e}}} \cdot \exp\frac{\text{e}\Phi_\text{p}}{\text{k}_\text{B}T_\text{e}} = \Gamma_\text{e} = Z\Gamma_\text{i} = f\, n_{\text{i},\infty}\sqrt{\frac{Z\text{k}_\text{B}T_\text{e}}{m_\text{i}}}$$

$$\Phi_\text{p} = \frac{\text{k}_\text{B}T_\text{e}}{\text{e}} \cdot \left(\ln\frac{2\pi m_\text{i}}{m_\text{e}} + \ln f\right)$$

Where f is the ion flux onto the probe in SCEPTIC's units. Please note that the above equations are only correct for a Maxwellian electron velocity distributions. Furthermore $n_{\text{e},\infty} = n_{\text{i},\infty}$ is assumed, which is correct in most cases, but might be wrong when there is no quasi-neutrality (e.g. in the sheath of a plasma). In this case the potential would change by an additional $\Delta\Phi_\text{p} = \frac{\text{k}_\text{B}T_\text{e}}{\text{e}} \cdot \ln\frac{n_{\text{i},\infty}}{n_{\text{e},\infty}}$. This potential is used on the inner boundary. To avoid too fast and strong changes of the dust potential underrelaxation is used. Because ions that are accelerated by a changed potential must travel to the dust probe fluxes react only inertly. This means heavy oscillations can occur until an equilibrium is reached. This and the implicit use of Boltzmann electrons makes it impossible to simulate charging dynamics with SCEPTIC.
If one is interested in the behaviour of an insulating dust grain, the flux is counted

separately for all inner cells. A separate potential is then calculated for all inner grid points with the same equation as in the conducting case.

3.3.5 Particle motion

For convenience, particles' positions and velocities are stored and updated in Cartesian coordinates. For this purpose, firstly the electric field at the particle's position is calculated from the mesh potential in spherical coordinates and then converted. Then, pushing is performed by modifying the velocity and then the position. It is possible to change the timestep or to enable sub-cycling for particles close to the dust.
If particles leave the domain at the inner boundary (i.e. they get absorbed), the crossing time and place is determined. The particle is counted as in-flux for the corresponding dust segment. Immediately after absorption a new particle is created at the domain edge and pushed for the remaining fraction of the timestep (using the sub-cycling routine). Particles leaving the domain on the outer boundary are reinjected after the complete timestep (or sub cycle if used).

3.3.6 Reinjection

For reinjection of ions many different methods of determining their velocity can be chosen. Most of them include Monte-Carlo inverse sampling from a distribution function. The simplest case is a Maxwellian distribution. For this thesis sampling from a Maxwellian shifted by the drift velocity was used. The most sophisticated approach is to assume ions that are injected from a shifted Maxwellian at infinity and accelerated in the spherically symmetric potential mentioned in section 3.3.4 [29]. The according distribution functions are calculated analytically and are only valid in a collisionless plasma.
In the mode used for this thesis, cumulative flux distributions are calculated for all boundary cells. This is done by integrating the flux into the domain over the velocity distribution function on all boundary cells. Location (θ) and velocity components parallel as well as orthogonal to the flow can then be selected from these distributions via Monte-Carlo sampling. Angle $\varphi \in [0, 2\pi)$ – needed for specifying the three dimensional location – is randomly generated and the other tangential velocity component is selected directly from the (cumulative) velocity distribution function at a given v_θ.

3.3.7 Collisions

The only collision type implemented in SCEPTIC is charge exchange between ions and electrons. If enabled a collision frequency ν is set at the beginning of the simulation. This frequency is used for all particles independent of their velocity. If a

particle is moved for the first time in a step, the time t_{coll} until the it collides is randomly selected by sampling from $R = \exp(\nu t_{\text{coll}})$ with a random number $R \in (0,1)$. If this happens during the current timestep the particle is pushed for the time t_{coll}. Then, its velocity is reset to the randomly selected neutral velocity. These are distributed according to a non-shifted Maxwellian [30].

4 Electronegative Plasma

4.1 Description of the experiment

Negative ions have major influence on the dynamics in a plasma. In 2010 Küllig et al. presented a method for measuring negative ion densities with minimally invasive techniques [10]. They used 160 GHz microwave interferometry to determine the electron density of a capacitively coupled O_2 plasma. They also added a frequency-doubled Nd:YAG laser, which was adjusted in such a way that both beams cross defining a diagnostic volume. The experimental setup is depicted in figure 4.1. The photons emitted by the laser have an energy of 2.3 eV. This is more than the electron detachment energy 1.46 eV of the O^- ions. When the laser is provided with enough power, all negative ions along its beam emit the electron with the lowest binding energy. This local increase of electron density can be measured by the interferometer beam and from the difference one can calculate the density of O^- ions in the unperturbed plasma. After the initial rise of the electron density a decay to the original equilibrium value is observed, because the source electrons from detachment disappear from the diagnostic volume.

Depending on the applied rf power, the plasma can establish two operational regimes. One of them with high and one with low electronegativity. After detachment the decay of the signal is much slower in the regime of higher powers. In this regime due to the lower electronegativity the electron source from detachment is much weaker compared to the regime of high electronegativity. That means that the systems with smaller perturbations take longer to equilibrate. For plasmas at pressures of 30 Pa equilibrium was reestablished after $\tau = 2 \ldots 5\,\mu s$ for high electronegativities (i.e. $\alpha > 2$) and $\tau = 70 \ldots 100\,\mu s$ for low electronegativities. The experimental data are shown in figure 4.2.
This experiment was simulated using the Particle-in-Cell to study the processes that lead to the relaxation of the system.

4.2 Modelling of the plasma

The simulation of the plasma was performed by a one-dimensional Particle-In-Cell code as described in section 3.1. For all runs the gas pressure was set to 30 Pa.

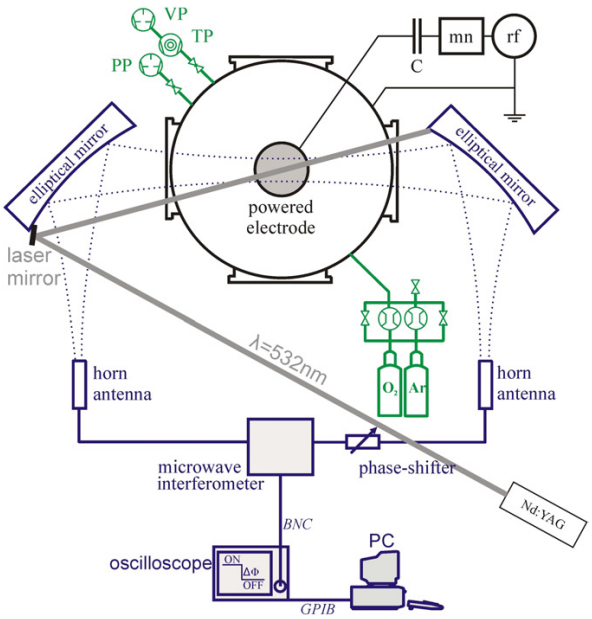

Fig. 4.1: Experimental setup of the negative ion detachment diagnostic experiment [10].

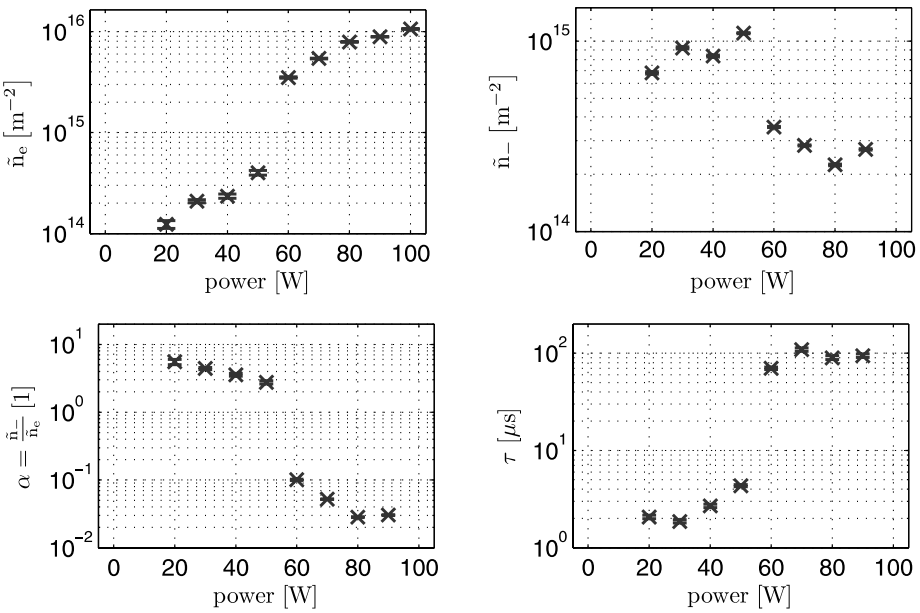

Fig. 4.2: Bulk densities, electronegativity and decay time constant as measured in the experiment [10].

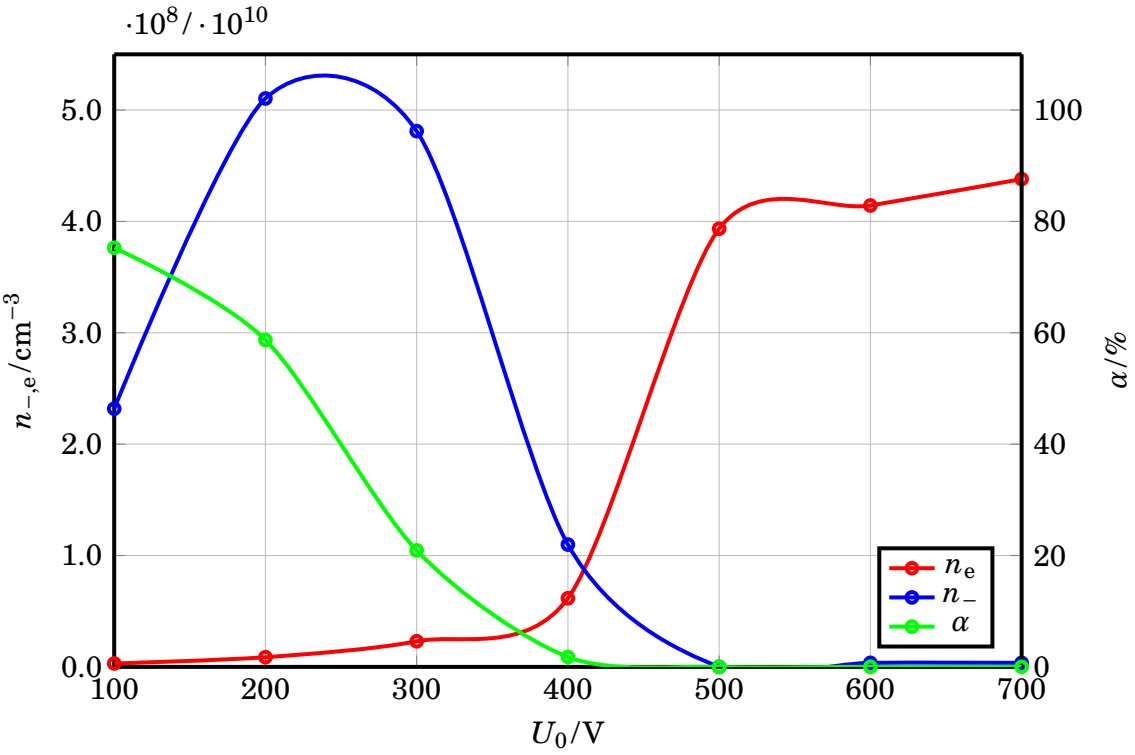

Fig. 4.3: Bulk densities and electronegativity for plasmas simulated at various driver voltages U_0.

Depending on the expected electron density (and therefore on the used grid size as discussed in section 3.1.2) the distance between the electrodes was about 4.6 cm. The left electrode was always grounded, while the right electrode's potential was harmonically oscillating around 0 V at a frequency of 13.56 MHz and varying amplitudes U_0.

To study the influence of plasma heating, simulations with a range of different driver voltages have been performed. The results are shown in figure 4.3. One can see, that the amount of positive O_2^+ ions and electrons increases at higher voltages, while the density of the negative O^- ions decreases. This behaviour is observed experimentally and occurs because of temperature changes in the plasma. Raising the driver voltage increases the plasma potential and the electric field close to the electrodes. Therefore, acceleration in the sheath become stronger. This leads to higher temperatures in the sheath and ionizations by electron impact become more likely – leading to more electrons and positive ions. In the bulk one observes the opposite trend. At the beginning electrons with higher temperatures are created, because of the larger electric field, but with increasing number of O_2^+ ions, more

collisions occur. These drain energy from electrons to ions, reducing the electron temperature. This lower bulk electron temperature is not sufficient to dissociate neutral molecules, resulting in a reduced production of negative ions.

The voltages chosen for simulations of the experiment are 200 V (because it is near the point of maximum O^- density), 350 V (because electronegativity is significantly lower there, while statistics are still acceptable) and 630 V (which was the highest voltage with enough negative ions to see their equilibration at still acceptable simulation times).

4.3 Implementation of the detachment

To simulate the perturbation I implemented a routine resembling the photo detachment process. It is integrated into the PIC cycle for the pulse length $t_{\text{pulse}} = 7\,\text{ns}$ of the real laser. In these steps in an area of $r_{\text{laser}} = 6.5\,\text{mm}$ around the center of the simulated system a number of O^- ions is randomly selected and deleted. For each of them a pair of an O radical and an electron with the same velocity and position are created. They immediately perform an inelastic collision where they gain a total energy of $\Delta E = 0.87\,\text{eV}$, which is the energy of a photon with 532 nm wavelength minus the binding energy of a O^- ion according to [31]. From the total energy of the laser pulse (0.4 J) one can calculate how many photons are generated each timestep. The probability that an arbitrary ion in the laser diagnostic volume loses its electron can be calculated from photon number per timestep, detachment cross section and dimensions of the cells – or one can just define a fraction of ions to be hit by the laser.
A real laser hits a three dimensional volume while PIC cells are only one dimensional in the used simulation. The cell length in the direction orthogonal to the beam and to x must be a constant value. Cells closer to the laser center have a larger fraction of their volume accessed by the laser. The chance of detachment for an ion grows linearly with the detachment volume in the cell. The fraction of the laser beam affecting a given cell can be calculated as

$$\frac{A_{i,\text{in cell}}}{A_{\text{laser}}} = \frac{\arccos(a) - \arccos(b) - a\sqrt{1-a^2} + b\sqrt{1-b^2}}{\pi}$$

with $a = x_{\min}/R$ the ratio of the distance between center of the laser and the inner boundary of the cell $x_{\min}$ over the laser radius R. b is the same as a, but for the distance to the outer boundary of the cell. This ratio multiplied by the detachment probability and the number of negatively charged super ions gives the number of detachment reactions for each step. I chose parameters to guarantee detachment of electrons from all negative ions, because the detachment diagnostics in the experiment was operating in such a regime.

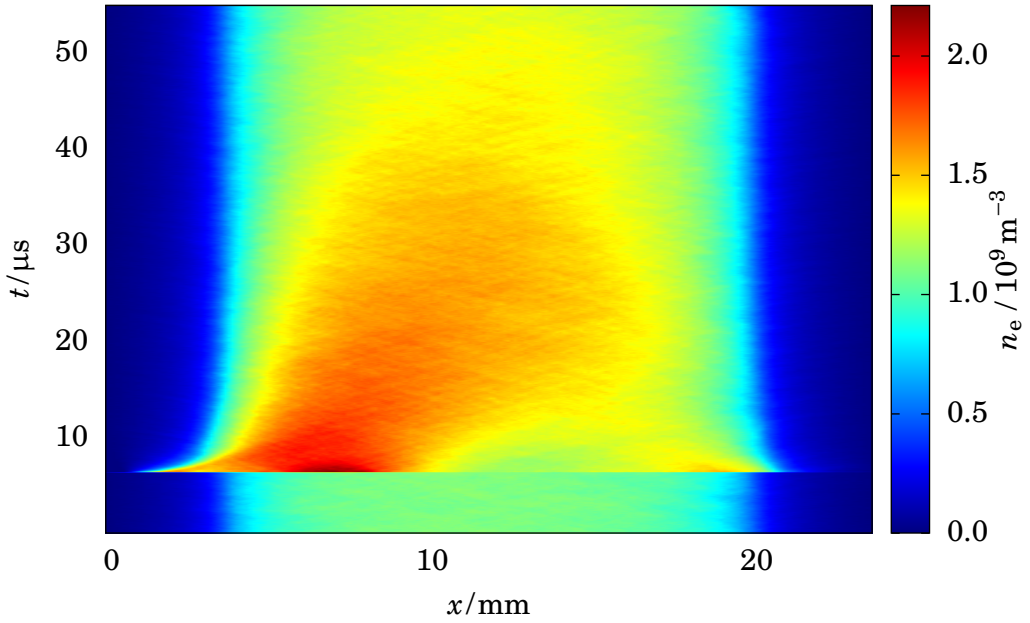

Fig. 4.4: Temporal development of the electron density in an Oxygen plasma after a large number of electrons was created in the bulk with an artificial photo detachment module. The plasma was heated with a driver voltage of 200 V.

4.4 Alternative detachment mechanisms

Some driver voltages produce very low O^- densities with electron densities several magnitudes higher. Because of this, very good statistics is needed to resolve variations in the density of both species after photo detachment. Increasing the number of simulated super particles has a notable impact on the runtime. I tried to circumvent this problem by creating an artificial diagnostic module, which allows to create new electrons without the consumption of negative ions. The amount of newly created electrons is not determined by the number of O^- ions. Therefore even for cases with very low negative ion densities at high electron densities, runs can be done with standard statistics.

4.4.1 Creation of solitary electrons

The naive approach to create photo-detached electrons is to simply create them at the position and velocity of randomly selected neutrals. The location where this happens and the energy gained by the electrons is the same as for the physically correct process.
As seen in figure 4.4, the problem with this concept is, that the electrons are carried

away by the RF field immediately after their creation. As soon as they reach one of the sheaths, they are decelerated by the strong electric field. This results in a higher electron density at the edge of the plasma. Many of the electrons ionize neutrals while others simply leave the plasma. Quasi neutrality is restored very fast. Later, this group of additional electrons and ions diffuses back into the bulk or out of the plasma. Since the bulk density temporarily returns to its old value within less than one RF cycle and increases again later on. This approach is an unsuitable alternative for the correct detachment mechanism, because it produces such artifacts.

4.4.2 Creation of electron-ion pairs

The biggest deficit of the previously presented approach is that it does not provide quasi-neutrality. If positive charges are created to confine the electrons an analysis of the temporal density development becomes possible. An intuitive way to do this is to perform ionizations of neutrals instead of just creating the electrons. The energy added to the resulting particles is $\Delta E = 0.87\,\mathrm{eV}$ again – despite the fact that the binding energies for both approaches differ.
This approach manages to confine the electrons. However the lifetime of the perturbed state is about an order of magnitude longer compared to the physically correct detachment mechanism, due to the strongly enhanced electron-ion collisions. Therefore, physically correct detachment must be used.

4.5 Transport processes during relaxation

The effects of detachment on an Oxygen plasma can be seen most easily, when there is a high O^- density to provide detachable ions. Hence the description of the processes after detachment are explained for a discharge heated with a driver voltage of 200 V. This plasma has a bulk electronegativity of $\alpha = 45\,\%$, which was the highest value achieved during the simulations. An overview of the temporal development is given in figures 4.5 to 4.8.

Major effects are:

- A part of the newly detached electrons quickly leaves the perturbed area (figure 4.5).

- Shortly after detachment the positive ion density only decreases at the edge of the detachment region. An increase outside the detachment region is driven by the diffusion electrons due to quasi-neutrality constraint. Later, the density loss moves inwards (figure 4.6).

- After the detachment stops, the edge of negative ion density remains steep. These ions are regenerated at approximately the same rate everywhere in the perturbed area. They are not affected by the changing densities of other species everywhere outside this region (figure 4.7).
- An electric field forms at the edge of the detachment zone and drifts inwards later. In addition, a smaller electric field drifts outwards from the same position (figure 4.8).

To explain the reason for this behaviour, all densities and the potential close to one edge of the detachment zone are plotted in figures 4.9 to 4.12.
In the beginning quasi-neutrality is guaranteed everywhere and the potential is approximately the same in the bulk (figure 4.9) – this holds true even when the first electrons are detached. There is however a steep gradient in electron and O^- density, which soon leads to electrons diffusing to the outside (figure 4.10). The O^- ions are much more immobile and do not show any visible diffusion behaviour. As soon as the first electrons have moved, the charge density gets negative just outside and gets positive just inside at the edge of the detachment region (figure 4.10). This charge separation creates a potential difference of $\Delta\Phi \approx 0.6\,\mathrm{V}$. This slows down the electrons and is enough to accelerate an O_2^+ ion by

$$\sqrt{\frac{2e\Phi}{m_+}} = 1895\,\frac{\mathrm{m}}{\mathrm{s}}$$

Investigating the slope of the escaping electrons in figure 4.5 (or of the positive ions in figure 4.6) reveals that their velocity is about $2200\,\frac{\mathrm{m}}{\mathrm{s}}$. This indicates ambipolar diffusion with the positive ions as the limiting factor in electron motion. Dividing the laser radius by the ambipolar velocity results in a characteristic transport time of about $3.0\,\mu s$, which is already in the range of relaxation times measured in the experiment and thus should be taken into account.
Because the resulting ambipolar electric field is very local (e.g. between $x = 8.4\,\mathrm{mm}$ and $x = 8.7\,\mathrm{mm}$ in figure 4.10) it can only affect ions in a small region at the edge of the detachment zone. This explains why the significant O_2^+ density reduction happens exclusively in this small strip shortly after detachment. Because very few of this field reaches into a region where there are still negative ions left, they will hardly be pulled into the depleted region. The effects of free O^- transport near the edge of the detachment region can be seen as a reduced slope e.g. in figure 4.11. In the same figure it also becomes visible, why these diffusing ions are not further accelerated into the detachment region: The removal of positive ions (e.g. around $x = 8.6\,\mathrm{mm}$ in this figure) as well as the electrons in outer regions of the perturbed area shifts the charge density bump inward. Accordingly, the ambipolar field shifts. The homogeneously rising O^- density all over the depleted area clearly indicates, that the regeneration must be a volume process – as was already suggested in the paper by Küllig et al. [10].

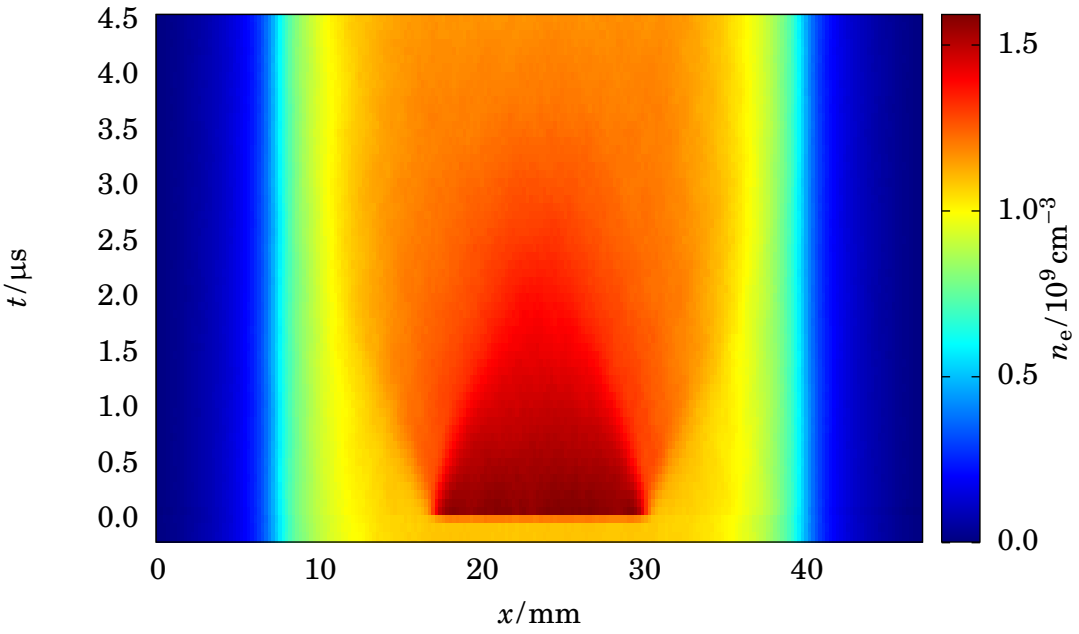

Fig. 4.5: Temporal development of the electron density in an Oxygen plasma heated with 200 V. Photo detachment was performed at $t = 0$.

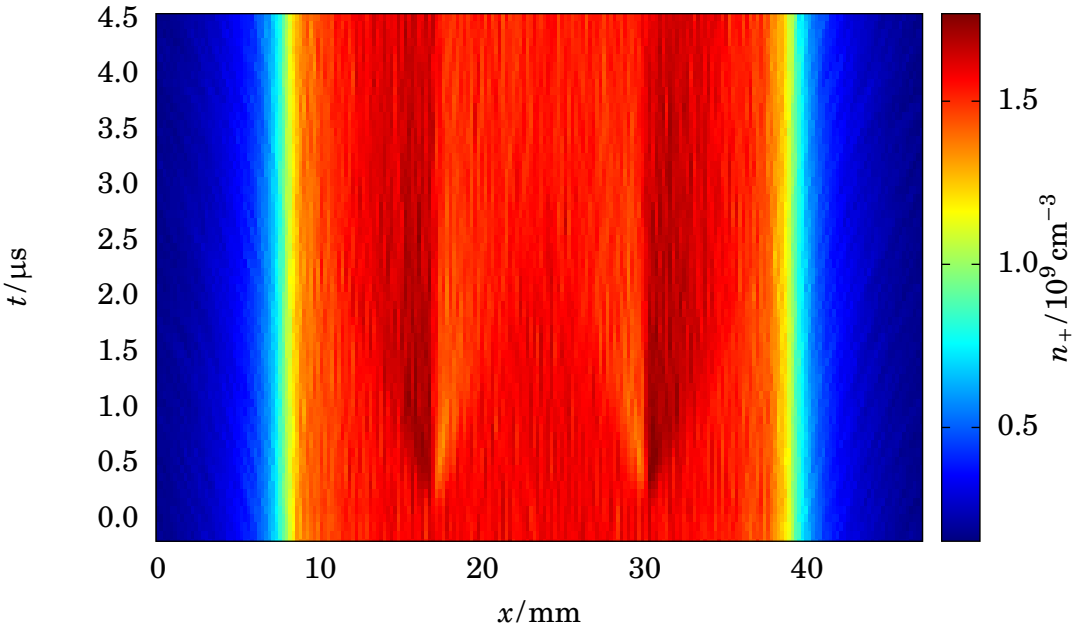

Fig. 4.6: Temporal development of the O_2^+ density in an Oxygen plasma heated with 200 V. Photo detachment was performed at $t = 0$.

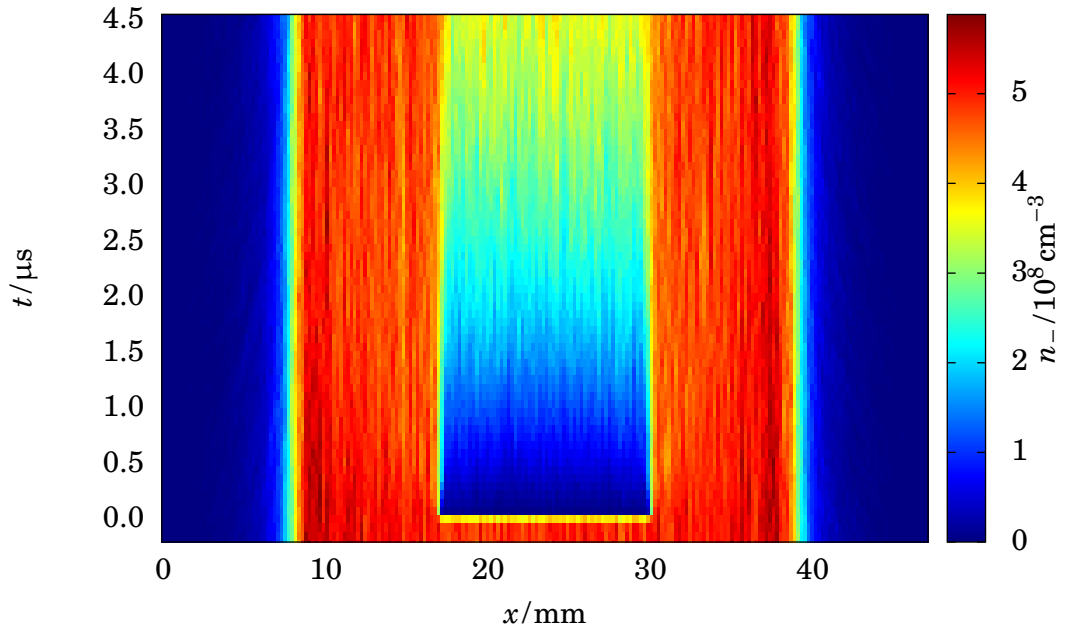

Fig. 4.7: Temporal development of the O^- density in an Oxygen plasma heated with 200 V. Photo detachment was performed at $t = 0$.

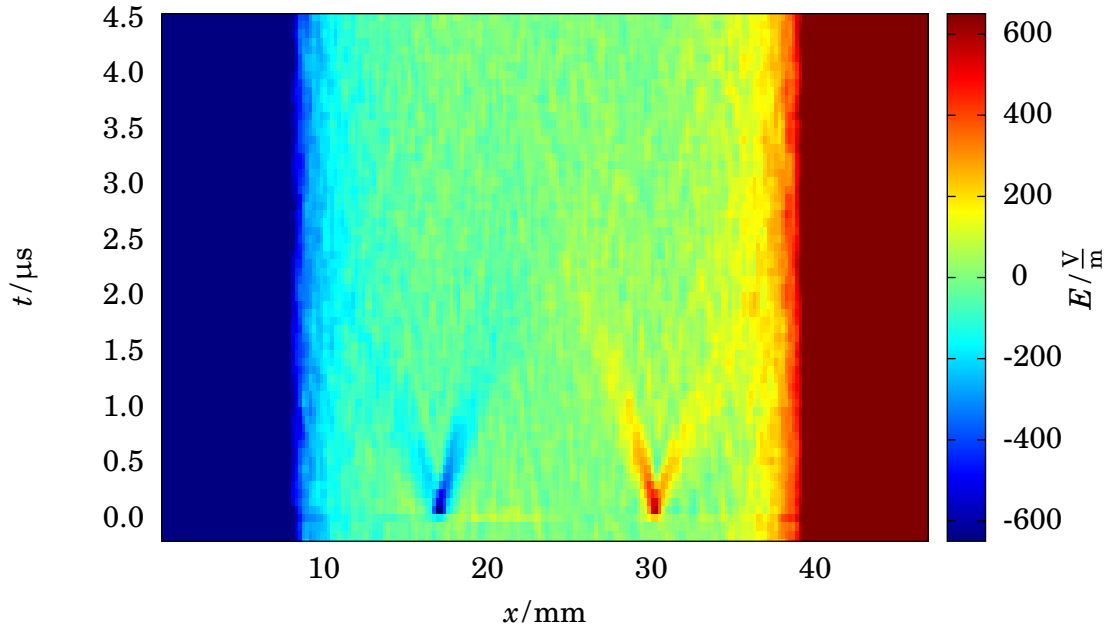

Fig. 4.8: Temporal development of the electric field in an Oxygen plasma heated with 200 V. Photo detachment was performed at $t = 0$.

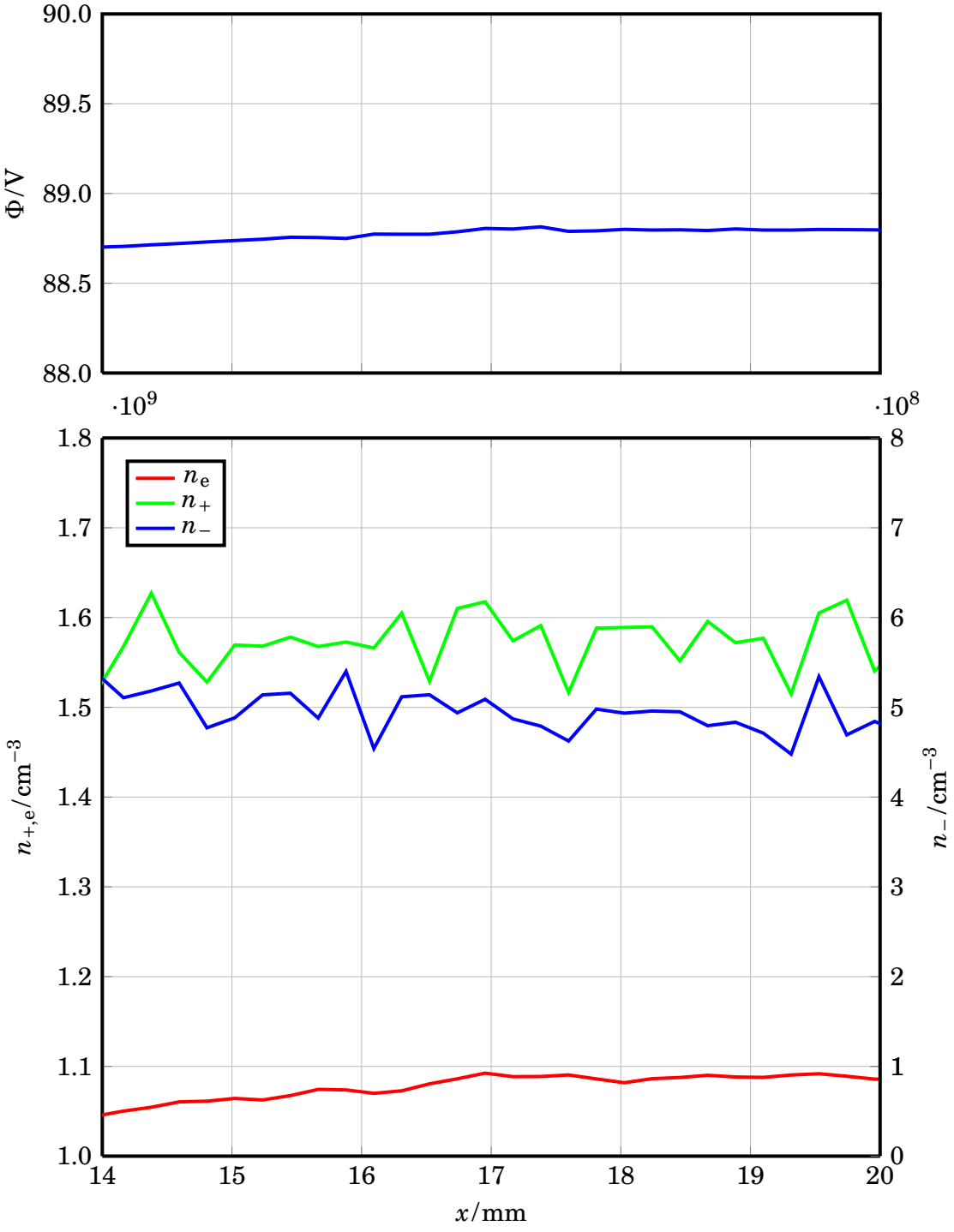

Fig. 4.9: Potential, electron and ion densities near the left edge of the detachment region before detachment was performed.

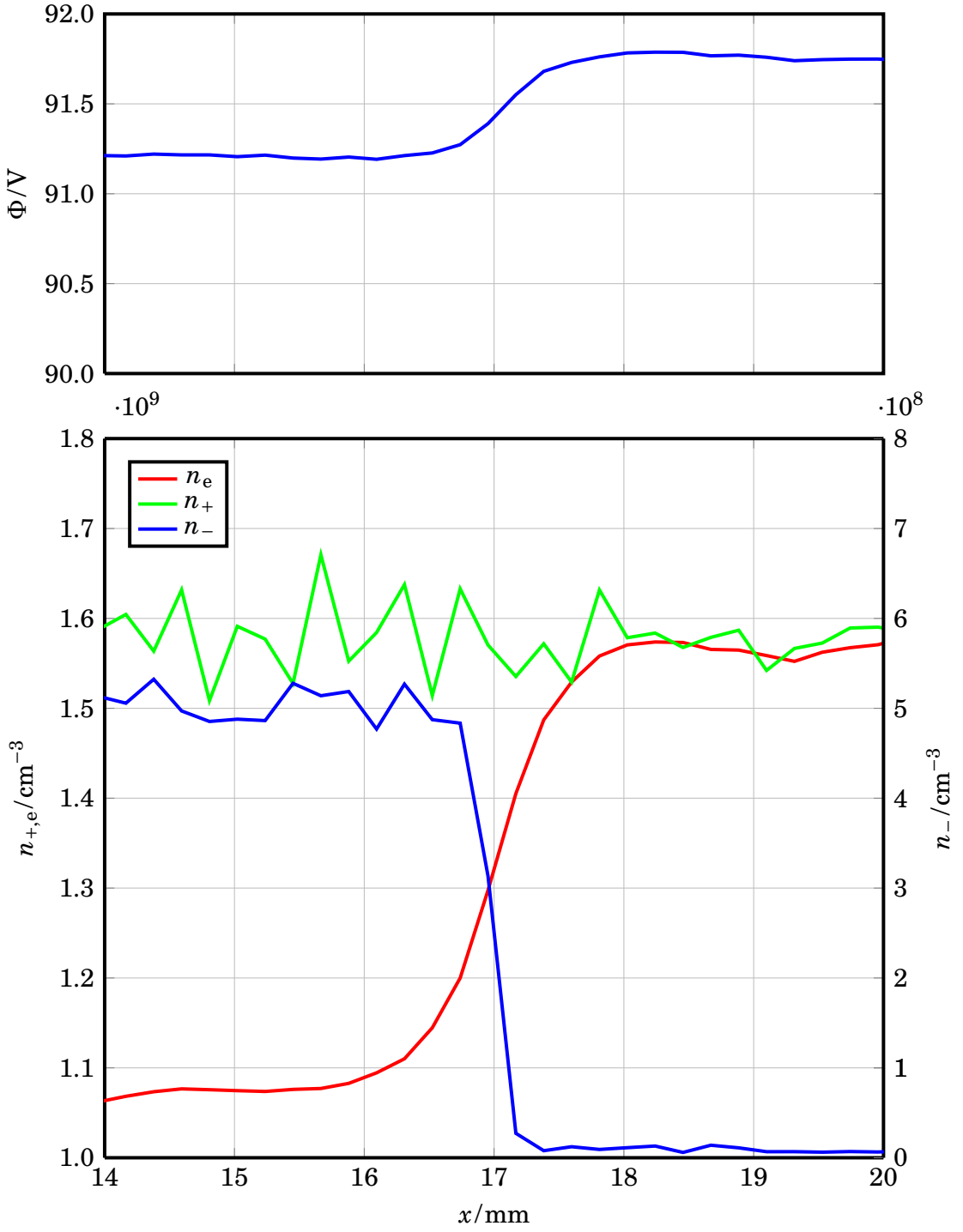

Fig. 4.10: Potential, electron and ion densities near the left edge of the detachment region shortly after detachment was performed.

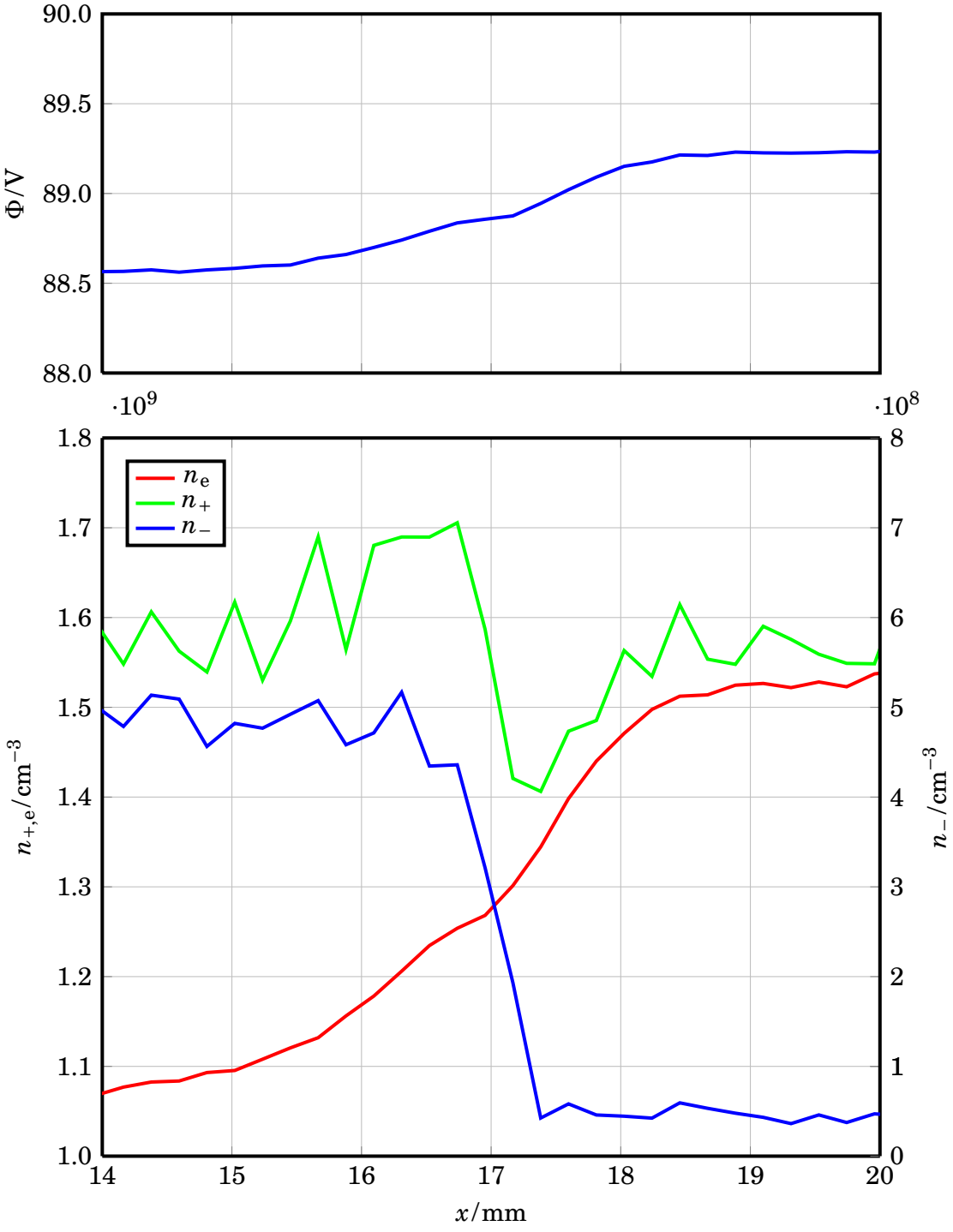

Fig. 4.11: Potential, electron and ion densities near the left edge of the detachment region five RF cycles (0.4 µs) after detachment was performed.

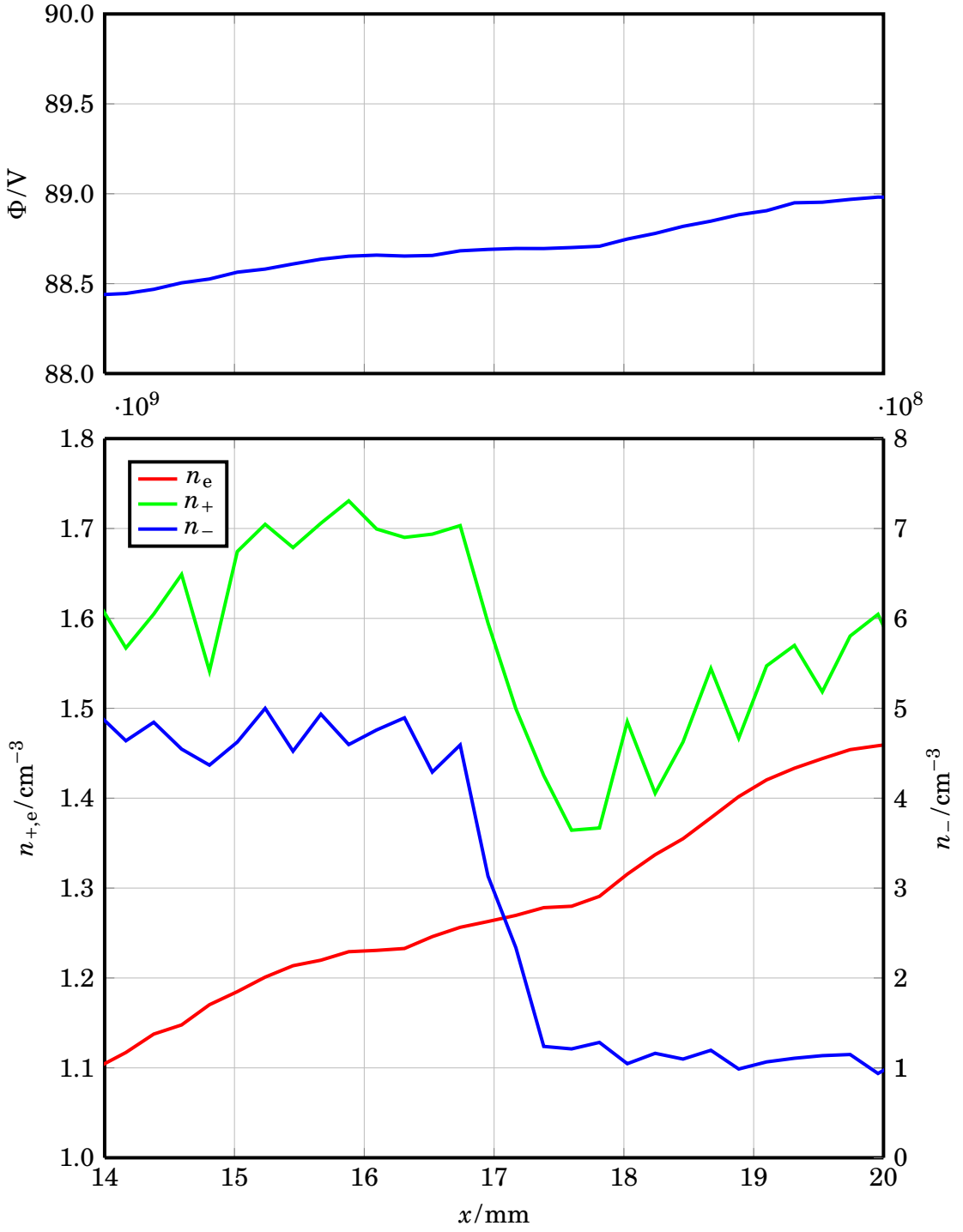

Fig. 4.12: Potential, electron and ion densities near the left edge of the detachment region twelve RF cycles (0.9 µs) after detachment was performed.

4.6 Bulk processes during relaxation

Analyzing the bulk processes is possible by counting all reactions between two simulation timesteps and rescaling them to units of density (of produced particles) per time (between two steps). Dividing these rates by the density of one of the reagent species gives effective rate coefficients.

Negative ions are produced everywhere in the bulk by dissociative attachment of electrons. As can be seen in figure 4.13, this only changes shortly after detachment. The reason for this is quite surprising. Although detached electrons have a higher temperature due to the energy gained from the laser the overall electron temperature in the inner bulk decreases. This happens, because fast particles are the first to leave the region, while slower particles stay. After about three RF cycles the dissociative attachment rate restores to its old rate of $\dot{n}_{-,\mathrm{prod}} = \widetilde{K_\mathrm{a}} = 1.5 \cdot 10^{14}\,\mathrm{cm}^{-3}/\mathrm{s}$. There are two concurring processes, that influence the O^- production rate. On the one hand the decreasing number of electrons reduces the production rate, but on the other hand the return of higher energetic electrons makes detachment more efficient, which leads to stronger ionization. These two processes balance nearly perfectly.

The equilibration of the negative ion density is possible, because the reactions consuming O^- ions are proportional to their density. The reaction limiting the density of negative ions is detachment on neutrals. All other reactions destroying O^- ions can be neglected. This means a linear slowdown of ion regeneration, because density and temperature of the background gas do not change. Detachment occurs at an effective rate of $k_\mathrm{d} = 3.1 \cdot 10^5\,\mathrm{s}^{-1}$, which is constant over time. The above considerations lead to the differential equation

$$\dot{n}_- = \widetilde{K}_\mathrm{a} - k_\mathrm{d} n_-$$

with the solution

$$n_- = \frac{\widetilde{K}_\mathrm{a}}{k_\mathrm{d}} \cdot \left(1 - \mathrm{e}^{-k_\mathrm{d} t}\right).$$

This suggests that the time the plasma takes to recover from the induced detachment, $\tau_\mathrm{d} = k_\mathrm{d}^{-1} = 3.2\mu\mathrm{s}$ only depends on the neutral detachment rate. Larger or smaller production rates only change the equilibrium density, but not the time needed to reach it. One should also note, that higher detachment rates lead to faster equilibration only due to the equilibrium being at lower density. They do not accelerate ion production.

Finding an analogous equation for the electron density is only possible with one more approximation. Electrons are not only produced in the bulk by detachment on neutrals, but also via ionization in the sheathes. For the derivation of this differential equation it is assumed, that there are no net fluxes between bulk and outer

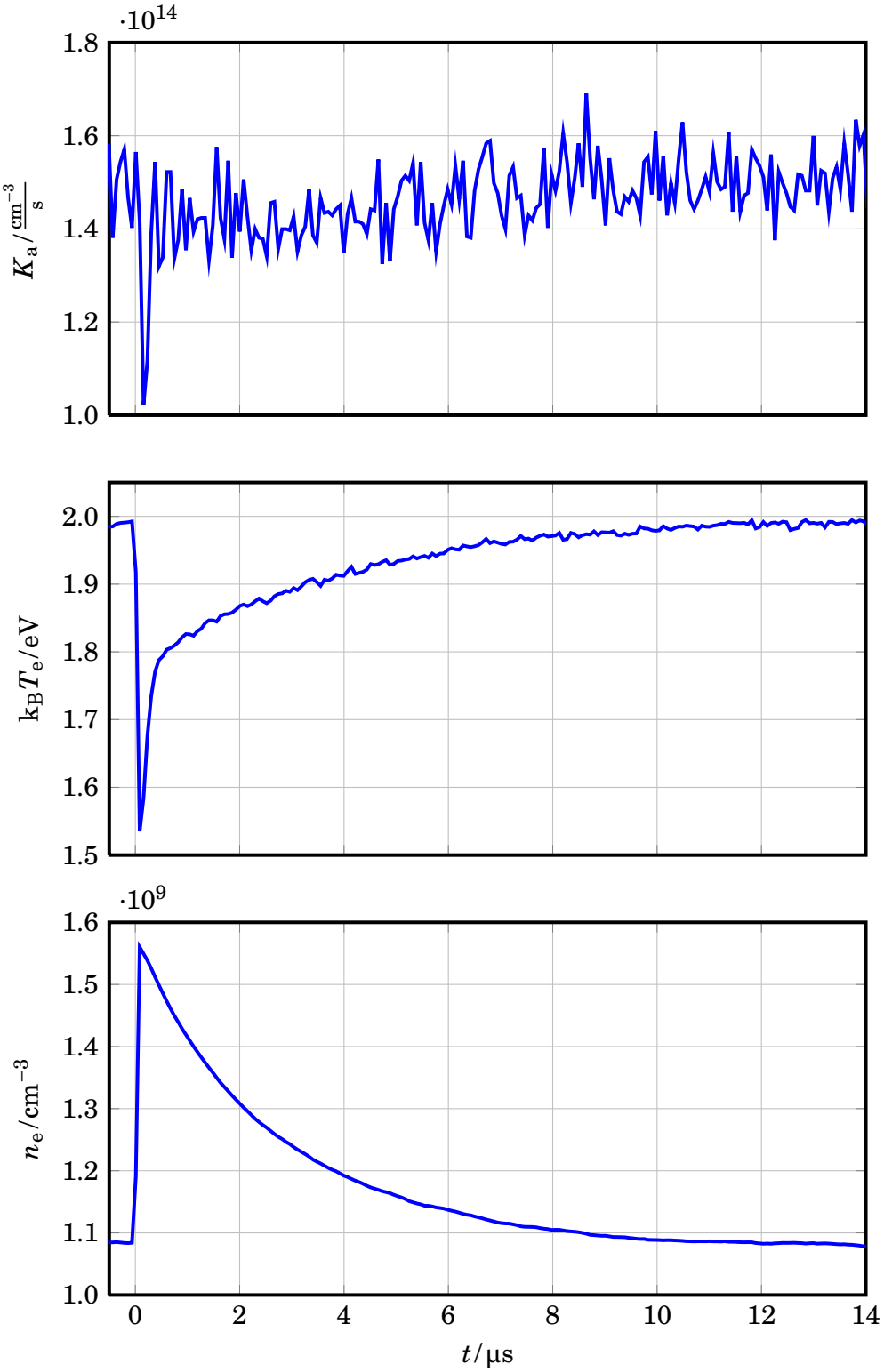

Fig. 4.13: Production rate of negative ions in a 200 V plasma shortly after detachment. Electron temperature and density are plotted for comparison.

areas. This is not really true except for equilibrium. This approximation leads to the differential equation

$$\dot{n}_\mathrm{e} = k_\mathrm{d} n_- - \widetilde{K}_\mathrm{a} = -\widetilde{K}_\mathrm{a} \cdot \mathrm{e}^{-k_\mathrm{d} t}$$

with the solution

$$n_\mathrm{e} = n_{\mathrm{e},0} + \frac{\widetilde{K}_\mathrm{a}}{k_\mathrm{d}} \cdot \mathrm{e}^{-k_\mathrm{d} t}$$

The equilibrium electron density $n_{\mathrm{e},0}$ cannot be calculated here, because it is defined by sheath and transport processes. The latter ones might lead to an electron density that is temporarily lower than expected with this model.

The considerations given in this section are only valid, if the production rate of negative ions stays approximately constant. This behaviour was observed in all three simulated regimes with the exception of the first three rf periods for the 200 V case. In fact the O^- production breakdown shortly after detachment might have a longer duration for higher O^- densities, when more electrons are detached and leave the region. The small period of decreased dissociative attachment rates does not affect the model, because nearly no ions are produced in this phase. Regeneration just starts a bit later. Another assumption for this model is, that neutral detachment only depends linearly on negative ion density. This is a reasonable assumption as long as neutral and ion temperatures are approximately constant, which is expected and observed.

4.7 Comparison of regeneration processes at different voltages

The detachment was also simulated with driver voltages of 350 V and 630 V. Because there are only few ions available for detachment the initial perturbation is small and its effects are often masked by statistical noise.

In figures 4.14 to 4.16 the temporal development of O^- and electron density after detachment can be seen. To minimize the effect of possible drifts, only density differences between simulations with and without detachment have been used. The values are averaged over the whole detachment region (solid lines) and over half of it (dashed lines). Especially, the temporal development of densities for the 200 V heated plasma (in figure 4.14) shows the different contributions from transport and reactions to reach equilibrium again. The nearly linear dependence at the start of both dashed lines is the bulk process of dissociative attachment, which produces negative ions at a constant rate. Neutral detachment is unimportant, because there are not many negative ions existing yet. This mechanism becomes

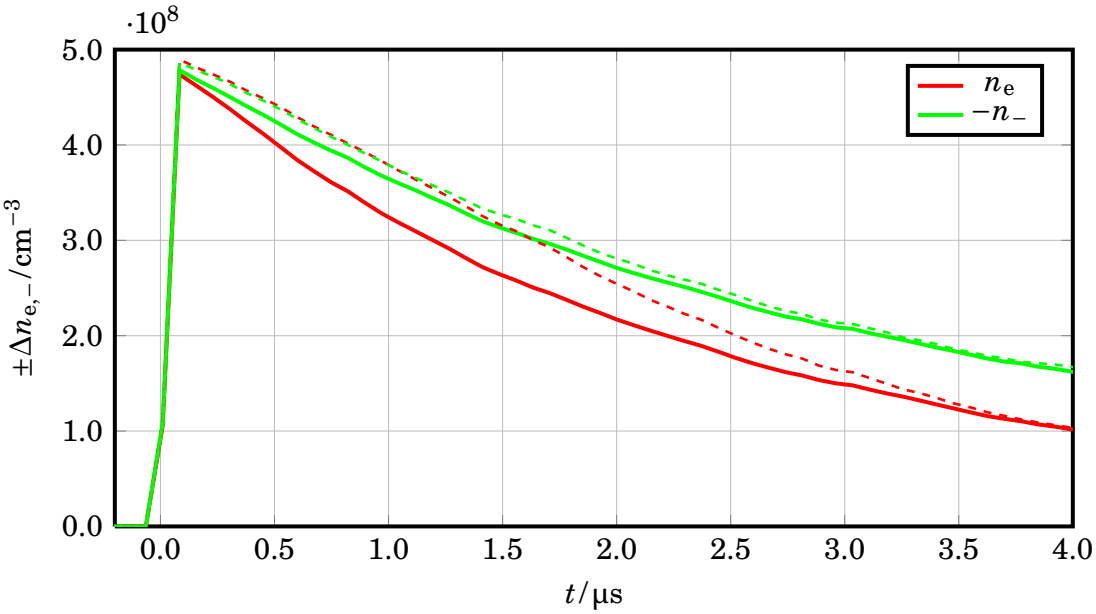

Fig. 4.14: Deviations of electron and negative ion density from their unperturbed values in an Oxygen plasma driven with 200 V.

important around 1.1 µs after detachment. The electron density still decreases at a linear rate, while the number of negative ions increases more slowly. No additional kink is visible in the graph of the electron density for the dashed line, because the ambipolar field is already very small when it arrives at the inner region of the bulk. The solid lines include transport effects. Therefore, a much faster decay of electron density is observed. O^- ions also travel into the region by diffusion, but to a much smaller extent. During the first microsecond the rate at which electrons leave the detachment area grows, probably because the electron density gradient gets broader and therefore electrons from a larger region get accelerated. Smaller gradients lead to smaller transport effects.

In the 350 V plasma (figure 4.15) the same effects can be seen. Because the initial O^- density is smaller deep inside the bulk the solid and dashed lines start at different points. The most notable difference to the 200 V case is, that even though electron transport becomes clearly visible, it very soon slows down until Δn reaches approximately the same value after about 3.2 µs. After this time electron and ion perturbations are equal. The slowdown is driven by the small amount of newly produced electrons, which diminishes diffusion. Since electrons get consumed by dissociative attachment, electrons must actually have diffused back into the region to replace those that left it shortly after detachment.
The initial breakdown in dissociative attachment could not be seen in this regime.

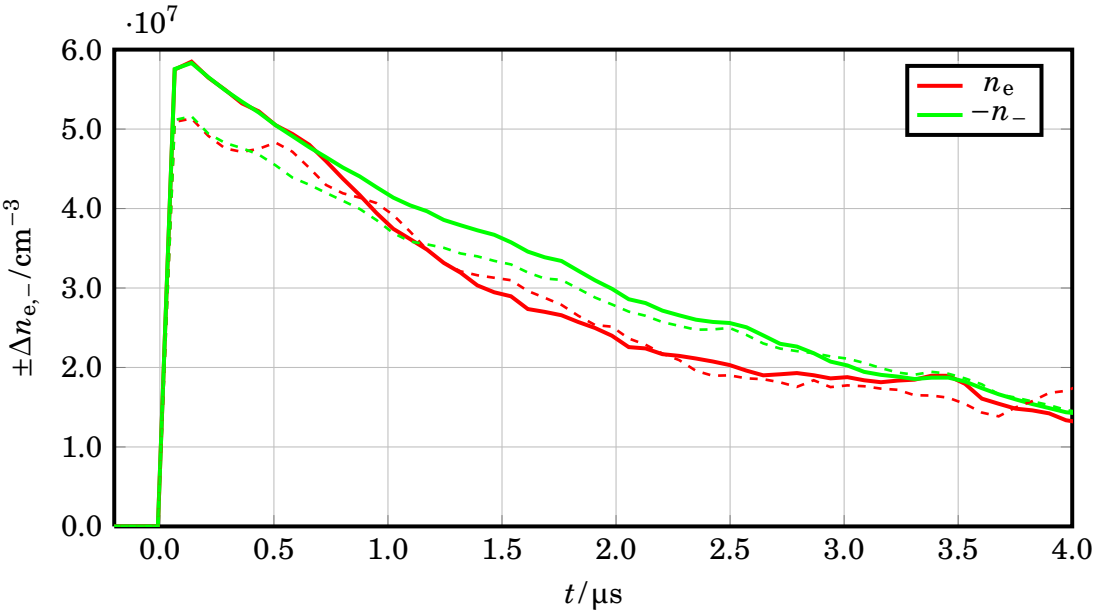

Fig. 4.15: Deviations of electron and negative ion density from their unperturbed values in an Oxygen plasma driven with 350 V.

A small temperature drop in the detachment region was visible, but production rates remained unchanged. Inverting this rate leads to an equilibration time of $\tau_d = 3.7\mu s$.

Because only few electrons from detachment increase their total number, statistical noise is quite large. In the plasma driven with 630 V (figure 4.16) the noise was so large, that no reliable information could be obtained. Negative ions show the same behaviour, that has already been described for the other simulations. On average the electrons follow this behaviour, which means that there is (nearly) no outward transport of electrons other than the normal transport that occurs due to the applied field. The negligible density increase gives no reason for the electrons to diffuse outwards. The equilibration time was measured to be $\tau_d = 3.2\mu s$.
The density deviation reached at times τ_d coincide quite well with the expected values of $\widetilde{n}_{max} \cdot e^{-1}$. The simulated effective rates for detachment on neutrals lie within a factor of five near the experimental results for high electronegativities, which lie between $6.2 \cdot 10^4 s^{-1}$ and $10.1 \cdot 10^4 s^{-1}$. The time constants are within 50 % of the experimental values (1.9 µs to 4.3 µs [10]).

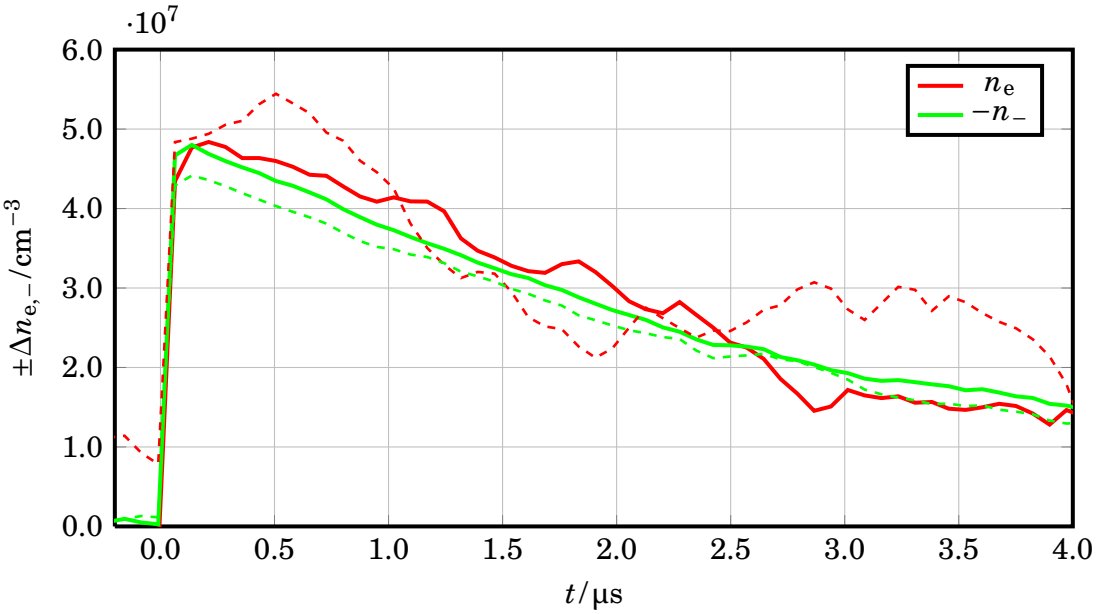

Fig. 4.16: Deviations of electron and negative ion density from their unperturbed values in an Oxygen plasma driven with 630 V.

4.8 Artificial amplification of collisions

The detachment simulation with highest electronegativity was repeated with modified transport. This was achieved by amplifying the cross sections of all elastic collisions (i.e. all collisions, that do not change a particle's species or dissipate energy) by a factor of 500. Results in figure 4.17 are as expected. All four graphs are approximately the same, so electrons are not transported and associative detachment is the only way to diminish their numbers. An unexpected aspect is, that the perturbation relaxes much faster with this modification and that the lines stay linear much longer. These effects occur, because the high energetic electrons, that were the first to leave the region by diffusion just stay inside the bulk. The resulting higher temperature leads to a larger number of generated O^- ions.

4.9 Interaction between bulk and transport processes

Küllig et al. [10] interpreted the decay of the perturbation as a volume process. The results presented here agree with this. Two assumptions entering their analysis are valid only for small electronegativities.
Firstly, the effective rate coefficients were assumed to be constant. This is not the

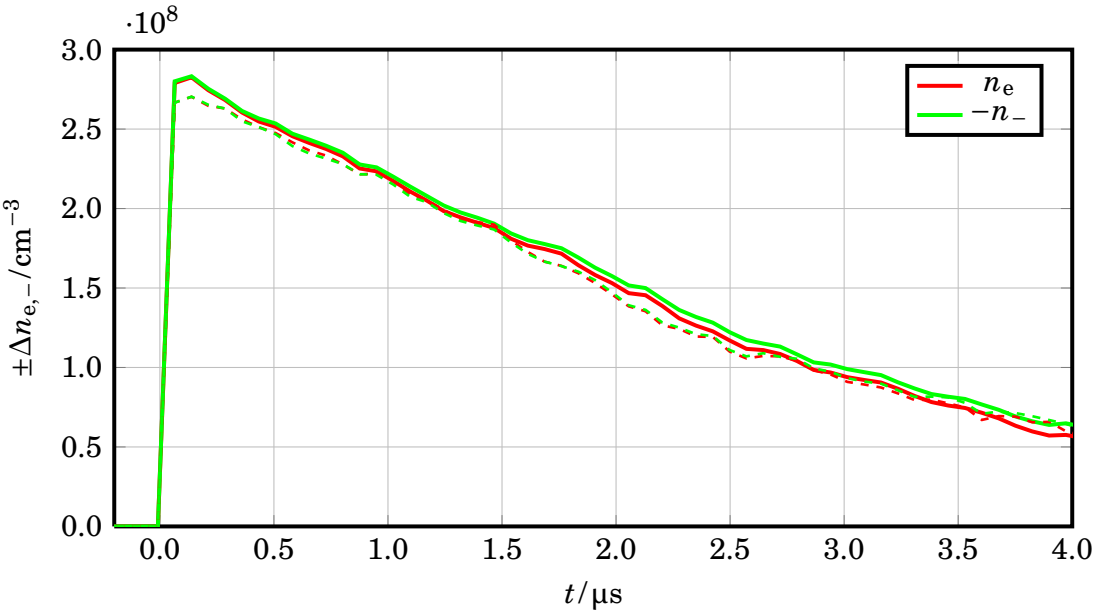

Fig. 4.17: Deviations of electron and negative ion density from their unperturbed values in an Oxygen plasma with amplified elastic collisions.

case, because the electron temperature lowers when highly energetic electrons leave the detachment region due to diffusion. In fact the rates were approximately constant, except for the short breakdown phase observed in the highest electronegativity case. This even lowered the rate. When this adiabatic cooling effect is lost at very low electronegativities, the perturbation in electron densities is also very small. The resulting dissociative attachment rate is therefore also nearly constant, which is the same as expected for a linear dependency.
Secondly they assumed that $n_e + n_- = n_+ = \text{const}$, but it actually changed especially at the edge of the region. This is an effect of electrons pulling O_2^+ ions outwards via ambiplor diffusion. These effects decrease with reduced electronegativity. Here, the smaller perturbation leads to smaller electron diffusion, resulting in less temperature decrease and weaker ambipolar fields. If less electrons leave the detachment region due to smaller perturbations, both approximations become true.

The simulated relaxation times are close to the experimental values at high electronegativities, because only those were accessible for the simulations. Studies of regimes with very low electronegativities were not possible, because runtimes needed to resolve the very low O^- density became far too long due to statistical limits. When testing an alternative detachment mechanism in section 4.4.2 one observed that high O_2^+ densities can lead to a very slow relaxation process. This timescale is similar to the long decay times observed experimentally in regimes of

high electron densities. As discussed before both relaxation processes are hindered by increased electron-ion collisions. Transport is decreased due to the lowered electron temperature. This effect was also visible with artificially amplified collisions in section 4.8. Transport processes could have an even larger effect in the experiment. Because the simulations used here are only one-dimensional, additional diffusion processes perpendicular to the rf field and profile dynamics are not included.

4.10 Synopsis

For this chapter electronegative Oxygen plasmas have been simulated. With increasing driver voltages electron and positive ion density increased while electron temperature and electronegativity decreased. This reproduces the experimental trend. A virtual diagnostics of electron detachment was introduced to understand this experimental method. The plasmas were perturbed by this electron detachment from all O^- ions in a region in the bulk. It was found, that the relaxation process is dominated by volume reactions. At higher electronegativities, the influence of transport processes became visible. This influence has two contributions: a direct one by electrons leaving the detachment region and an indirect one by adiabatic cooling of the electron temperature and therefore impeding dissociative attachment.
Simulated relaxation times were close to those measured in experiments with high electronegativities. Detachment in plasmas with very low electronegativities could not be studied, because the computational effort due to statistical restrictions was too high. It was however possible to observe significantly longer decay times at higher O_2^+ densities, when using an alternative detachment diagnostic with artificially increased transport. Such transport processes perpendicular to the axis not resolved in the 1D model can become dominant in the experiment explaining the much longer decay times observed for low electronegativities at high electron densities.

5 Dusty Plasma

When simulating any physical system, one can use different approaches, each of which has its own advantages and disadvantages. In this chapter results from the fully kinetic P3M code described in section 3.2 are compared to results from the hybrid code SCEPTIC (described in section 3.3).
Both codes are used for the simulation of dusty plasmas, but have different priorities. P3M strives to simulate the system as self-consistently as possible. It simulates the whole plasma with its heating mechanisms and models a wide variety of collisions. The dust itself has a charge, that is changed via the absorption of particles. It is even possible to use multiple ion species or to add multiple dust grains. The largest disadvantage is, that it is extremely memory and time consuming. One reason for this is the need to resolve the complete system size including electrodes with cells of typically half a Debye length. Also, electron motion needs to be resolved on the timescale of a fraction of the plasma frequency. It can take a week or more on eight nodes until the plasma has equilibrated and dust can be added. Also the number of particles near the dust is comparatively small. Having 1000 particles of each species within one Debye length of the dust is a usual number. To overcome this statistical limit using the ergodic hypothesis the ensemble average is replaced by a temporal average over a large number of timesteps (typically one million). This again increases the necessary runtime.
SCEPTIC is highly optimized for simulating the proximity close to one dust grain in the equilibrium. It only kinetically simulates ions, which allows much larger timesteps. This means that electrons are assumed to be Maxwellian. Their density is determined by a Boltzmann factor. Dust charging dynamics cannot be studied, because currents to the dust compensate each other by definition. The fact, that plasma parameters are not self-consistently calculated, but predetermined at boundaries is advantage and disadvantage at the same time. It allows to vary specific parameters easily, like the collision frequency. This would be very hard in a self-consistent model, because a separation of physics mechanisms is there not possible. Physics parameters needed for SCEPTIC have to originate either from more complex simulations or experiment. The biggest advantage of SCEPTIC is its short runtime, compared to P3M. Even with very high statistics single runs do not take much longer than a day on a single node. Depending on the plasma parameters and statistics it might even be minutes.

Benchmarks of both codes are therefore quite interesting to identify and quantify

differences allowing to judge the values of the two approaches. This is the topic of this chapter.

5.1 Sensitivity studies for a non-flowing Argon plasma

To study the influence of SCEPTIC's input parameters the runs have been performed on non-flowing Argon plasmas with ion temperatures that are within a factor of ten of the electron temperature. Because there is no comparison to a real experiment or other simulations the results are presented in SCEPTIC's dimensionless units within this section.

5.1.1 Finding a reliable domain size

Because SCEPTIC only simulates a small region, but not the whole system that determines the plasma parameters, it is important to choose the domain size large enough. In the case of boundary conditions chosen for this thesis, it must be large enough that quasi-neutrality is achieved at the outer boundary (which implies, that the potential there is the plasma potential). If this is not guaranteed either the floating potential is too high or the potential is approximately correct near the dust, but declines to plasma potential at a much too small spatial scale. The latter case would lead to an unphysically amplified electric field. It is also necessary to simulate a region that contains most of the particles reaching the dust, i.e. only a negligible fraction of particles near the outer boundary have a velocity that allows them to arrive at the dust. Not fulfilling this criterion leads to an underestimated ion flux and therefore a lower floating potential. The smallest domain size fulfilling these demands is called "collection range" within this thesis. It can be expected to be at a distance where the potential drop from plasma potential is small against the ion temperature. It must not be confused with the collection radius – the radius of the effective cross section a grain or probe with a given potential has for particles of a given species and velocity.

The influence of these concurring mechanisms was checked by varying the domain radius from 5 to 50 dust radii in Argon plasmas with $T_\mathrm{i} = T_\mathrm{e}$, $T_\mathrm{i} = 0.5 \cdot T_\mathrm{e}$ and $T_\mathrm{i} = 0.1 \cdot T_\mathrm{i}$. Simulations have been performed with Argon, because it was stated in [28], that SCEPTIC might face problems at ion temperatures below $0.1 \cdot T_\mathrm{e}$. The $T_\mathrm{i}/T_\mathrm{e}$ ratio for the Argon plasma that will be discussed in section 5.3 was much lower than this. Dust radii were chosen to be $r_\mathrm{d} = 0.02 \cdot \lambda_\mathrm{De}$ and $r_\mathrm{d} = 0.05 \cdot \lambda_\mathrm{De}$. The results in figure 5.1 show the same potential for all domain sizes in the thermal plasma. This means the standard domain size of $5 \cdot r_\mathrm{d}$ is sufficient for both dust sizes.

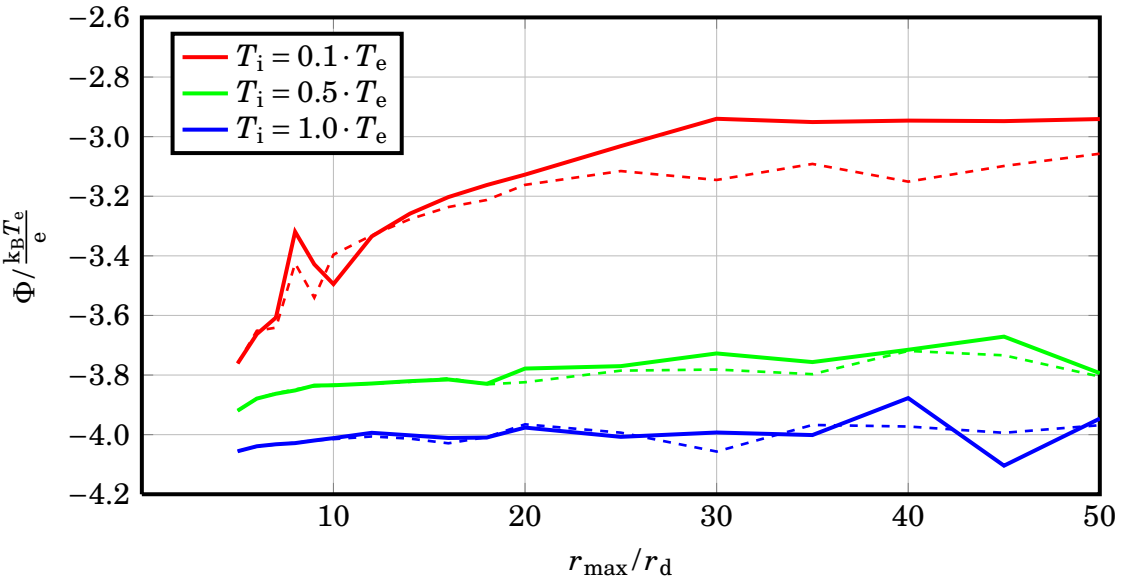

Fig. 5.1: Floating potentials of dust grains within an Argon plasma at different temperatures. Dust radii are $r_d = 0.02 \cdot \lambda_{De}$ (solid lines) and $r_d = 0.05 \cdot \lambda_{De}$ (dashed lines). Domain sizes r_{max} have been varied to identify the required minimum for this parameter.

When ion temperatures get lower, a larger domain size leads to higher floating potentials. This behaviour is best seen for $T_i = 0.1 \cdot T_i$. The collection range increases with falling ion temperature, because ions far away from the dust are less likely to escape its field then.
The different dust sizes for all temperatures are marked as different line styles. It can be seen, that potentials of both grains with equal temperature stop to rise at approximately the same point in the plot (e.g. around $30 \cdot r_d$ in the lowest energy case). This implies, that the collection radius does not only depend on parameters of the surrounding plasma but also scales with the size of the dust grain.
One can explain this behaviour by approximating the small dust particles as a spherical capacitor [32] with capacity $C_d \approx 4\pi\varepsilon_0 r_d$. With this approximation the potential around the grain can be written as:

$$\Phi(r) = \frac{Q_d}{4\pi\varepsilon_0 r} \cdot e^{-\frac{r}{\lambda_{Db}}} = \frac{C_d \Phi_d}{4\pi\varepsilon_0 r} \cdot e^{-\frac{r}{\lambda_{Db}}} = \frac{4\pi\varepsilon_0 r_d \Phi_d}{4\pi\varepsilon_0 r} \cdot e^{-\frac{r}{\lambda_{Db}}} = \frac{\Phi_d}{r/r_d} \cdot e^{-\frac{r}{r_d}\frac{r_d}{\lambda_{Db}}}$$

Close to the grain the potential depends only on the ratio $\frac{r}{r_d}$. Because the collection radius depends on the potential distribution and temperatures (which give the probability that a particle can leave the potential sink around the plasma), the same is expected for the collection range. Because the exponential term can only be neglected at distances much smaller than a Debye length, the potential relaxes

slightly faster for the larger grain, which explains the small difference in collection radius.

These considerations apply for collision-free plasmas. When collisions are introduced the collection radius tends to increase even further. Colliding particles loose the additional velocity obtained in the potential difference. The influence of regions far away from the dust becomes less important. Only the rate of particle injections at the boundary is important. Since this is automatically adjusted it might be possible to actually decrease the domain size. The only reliable way for testing, whether the simulated area is sufficient or not, is to repeat the simulation with a larger domain size and check for similar results.

5.1.2 Comparison of two different boundary conditions

Assuming the potential to be zero at the boundary is a very straightforward and transparent approach. Its disadvantage is that it is not possible to check whether this approximation is correct without changing the domain size (which is not necessarily correct). As was already described in section 3.3.4 SCEPTIC provides a method to apply boundary conditions which resemble those in a Yukawa potential without setting any fixed values.

The analysis from the previous section is repeated with this boundary condition for a dust particle with $r_\mathrm{d} = 0.05 \cdot \lambda_\mathrm{De}$ in plasmas at temperatures $T_\mathrm{i} = 0.1 \cdot T_\mathrm{e}$ and $T_\mathrm{i} = 0.1 \cdot T_\mathrm{i}$. The results are shown in figure 5.2. Even though boundary conditions are very different, the floating potentials for similar domain sizes are nearly equal.
For further investigations potential and density distributions of the $T_\mathrm{i} = 0.1 \cdot T_\mathrm{i}$ simulations at representative domain radii are analyzed. Potentials near the dust are shown in figure 5.3. Dashed lines use data from runs with $\Phi(r_\mathrm{max}) = 0$ and dotted lines use data with the symmetric approach. In the zoom for small distances both approaches lead to very similar floating potentials for the two larger domains. $r_\mathrm{max} = 25 \cdot r_\mathrm{d}$ is a sufficient domain size even though $\Phi(r_\mathrm{max}) \neq 0$). The same is true for the two results with $r_\mathrm{max} = 10 \cdot r_\mathrm{d}$. The zoom for large distances shows, that the symmetric approach is not necessarily a better choice than setting the potential to zero at the domain edge. Both blue lines are nearly identical, because Φ at the boundary is zero in both cases. These cases resolve the system sufficiently good, namely leading to practically identical solutions. As expected potentials are higher in runs with fixed boundary conditions, but differences to the well resolved case are nearly the same for both approximations.
Taking a closer look at the floating potentials shows that they are slightly higher, when boundary potentials are set to zero. For the smallest domain size this means

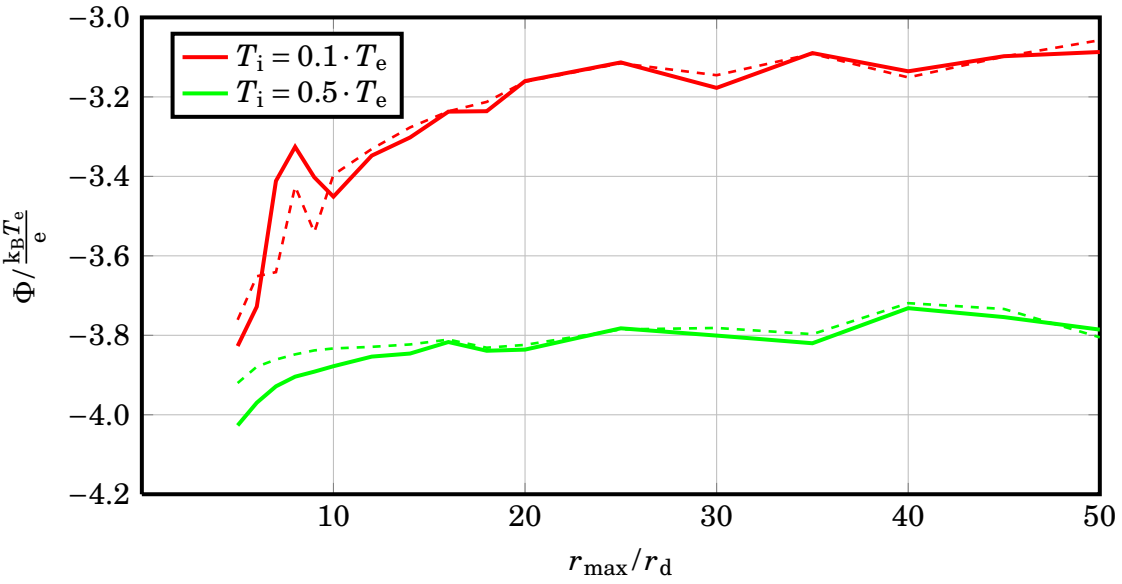

Fig. 5.2: Floating potentials of dust grains with radius $r_d = 0.05 \cdot \lambda_{De}$ in two different Argon plasmas with varying domain sizes r_{max}. Solid lines refer to "symmetric" boundary conditions. Dashed lines use $\Phi(r_{max}) = 0$

a difference of $0.05 \frac{k_B T_e}{e}$, which is about a fourth of the potential difference at the boundary. This makes perfect sense, because the lower potential difference in the symmetric case leads to less acceleration of the ions and therefore a smaller flux to the probe.
Ion densities around the dust are compared in figure 5.4. They also vary little between runs with different boundary conditions. In fact, densities within the first three dust radii are nearly equal, independent of domain size. The observation that $r_{max} = 10 \cdot r_d$ has ion densities below $n_{i\infty}$ is a numerical effect. Motion of low temperature ions is defined by their initial velocity. At the beginning of the run, this initial velocity leads to rather small fluxes to the probe. SCEPTIC will set a very negative potential, because it enforces strictly total currents to be zero (see section 3.3.4). This large electric field leads to increased acceleration and higher fluxes and the process will start over. This mechanism leads to density and floating potential oscillations before equilibrium is established.

5.1.3 Influence of the ion temperature

In this section the influence of ion temperature on an Argon plasma is investigated. Figure 5.5 shows floating potentials for different domain sizes at varyied ion temperatures. The line for the largest domain size shows, that higher floating poten-

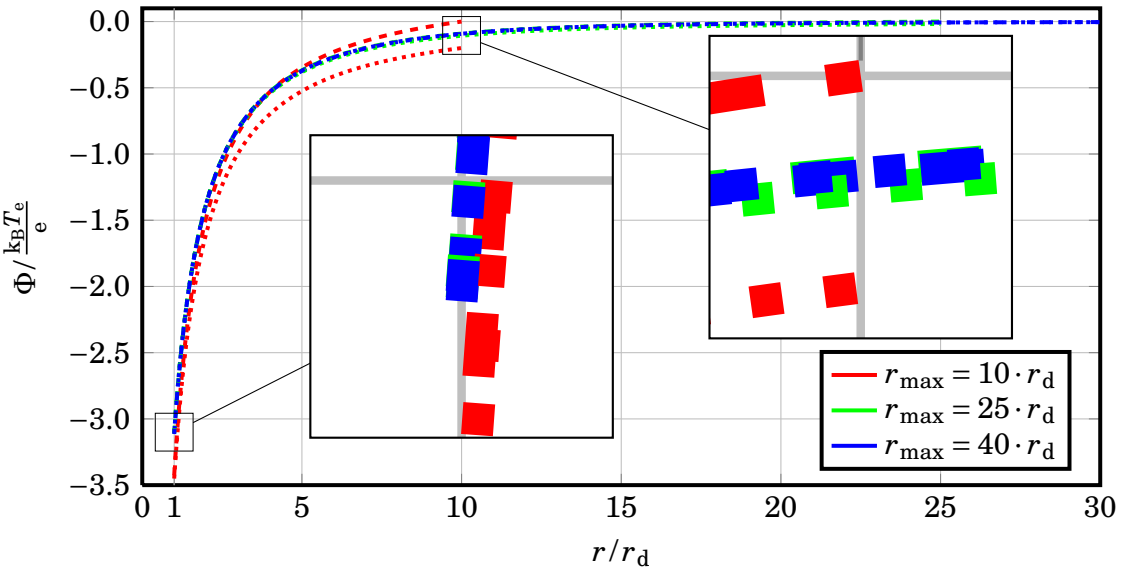

Fig. 5.3: Potentials around the same dust grain simulated with different domain sizes r_{max}. Dashed lines mean $\Phi(r_{max}) = 0$, dotted lines mean "symmetric" boundary conditions.

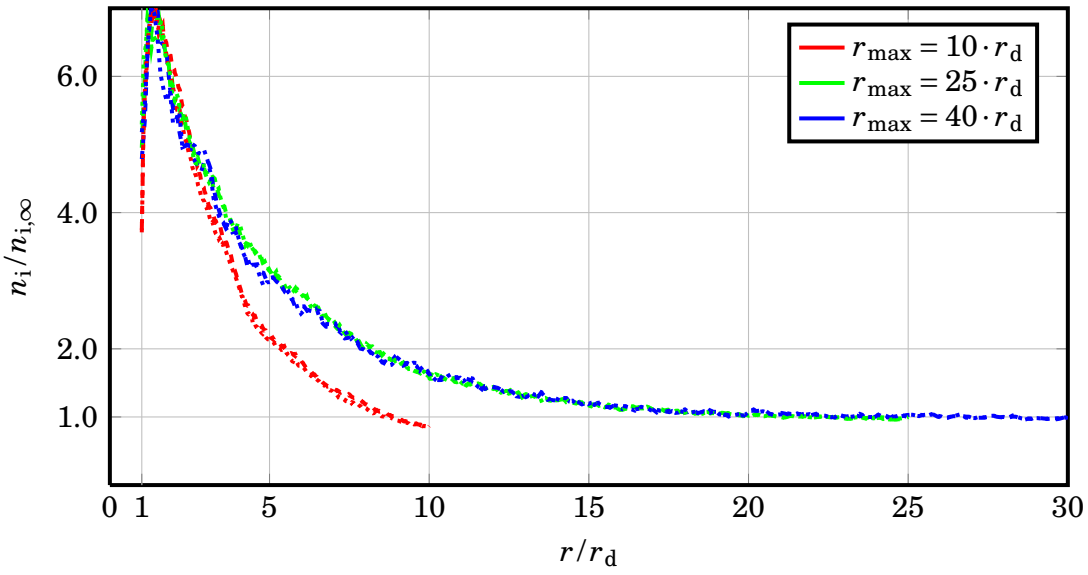

Fig. 5.4: Ion densities around the same dust grain simulated with different domain sizes r_{max}. Dashed lines mean $\Phi(r_{max}) = 0$, dotted lines mean "symmetric" boundary conditions.

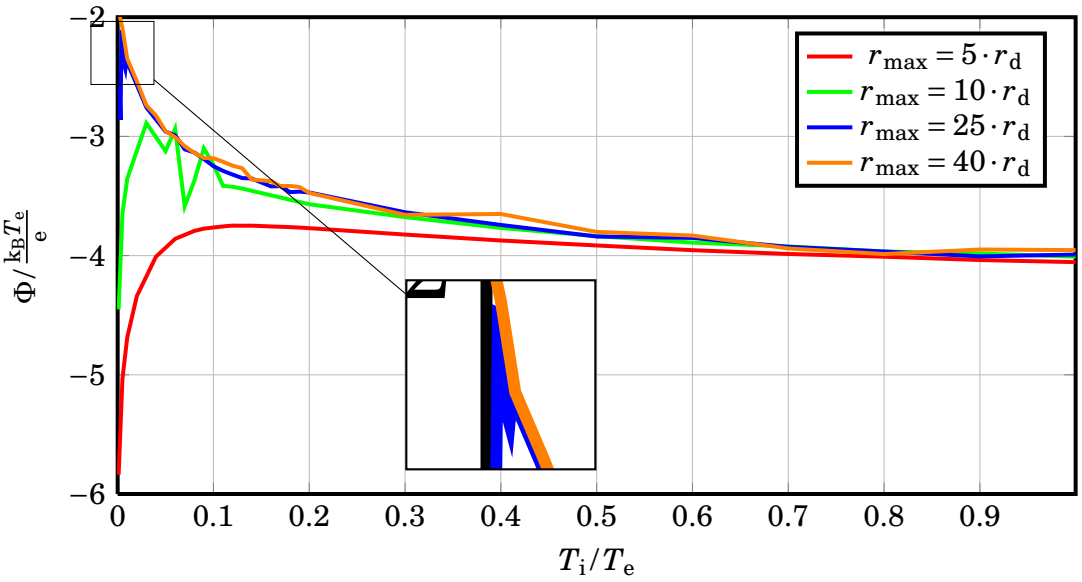

Fig. 5.5: Floating potentials of a dust grain with radius $r_d = 0.05 \cdot \lambda_{De}$ in an Argon plasma at different temperatures. Colors mark different domain sizes r_{max}.

tials are achieved, when ions are colder. This is the case, because more slower ions are absorbed from a dust grain of given potential, because they are less likely to escape it's electric field. Since the ion flow depends on the dust potential alone, this would lead to an unbalanced current. The potential rises and more electrons, but less ions, are absorbed – balance is restored.
For all smaller domain sizes there is a threshold temperature below which all floating potentials are much smaller than the respective potential for any simulation with larger domain size. Larger collection ranges lead to the correct floating potential at lower temperatures and vice versa. This means, that lower ion temperatures lead to dust potentials, because they increase the collection range. This supports the observations made in section 5.1.1.

5.2 Dust in the sheath region of a Hydrogen plasma

In 2007 Matyash et al. simulated the effects of micrometer-sized dust grains for a nearly isothermal Hydrogen plasma as used for fusion [26]. H^+ ions and electrons were injected with Maxwellian velocity distributions and an identical temperature

n_i	$8.3 \cdot 10^{11}$	cm^{-3}
n_e	$7.8 \cdot 10^{11}$	cm^{-3}
T_i	3.307	eV
T_e	9.467	eV
$u_\mathrm{d,i}$	$3.213 \cdot 10^{4}$	$\frac{\mathrm{m}}{\mathrm{s}}$
λ_Di	15	µm
λ_De	25	µm

Table 5.1: Plasma parameters of the P3M simulated Hydrogen plasma at the dust position.

of $T_\mathrm{e} = T_\mathrm{i} = 20\,\mathrm{eV}$ some distance away from the dust. The self-consistent equilibrium solution of P3M delivers the plasma parameters at the dust location (see table 5.1).

The simulated dust particles had sizes of $r_\mathrm{d} = 0.2075\,\mu\mathrm{m}$, $0.415\,\mu\mathrm{m}$, $0.83\,\mu\mathrm{m}$ and $1.66\,\mu\mathrm{m}$. When stationarity was reached their final charge scaled linearly with the dust radius and dust potentials were $\Phi_\mathrm{d} = -25.1\,\mathrm{V}$ in all cases. This is about 10 % higher than the floating potential expected from OML theory ($\varphi_\mathrm{d} = -27\,\mathrm{V}$).

5.2.1 Statistical range of floating potentials

A dust grain with $3.2\,\mu\mathrm{m}$ radius in the Hydrogen plasma described above was simulated with SCEPTIC multiple times. The simulation was stopped after a number of steps varying from the standard of 500 up to 10000 – the maximum value allowed by the original source code. In the beginning of the simulation the potential is likely to be wrong to some extent, because the potential is calculated from the particle flux onto the probe. This flux reacts slowly, because particles must travel to the probe first. Not even all of them are accelerated from the same potential, because of different transit times. Better values should be reached for longer simulation times, because they allow to finish the equilibration process. Furthermore, the domain size was varied from $r_\mathrm{max} = 5 \cdot r_\mathrm{d}$ to $20 \cdot r_\mathrm{d}$.

In figure 5.6 the dust potential at the end of the simulation is shown. The potential obtained from simulations with shorter end times deviates from the respective values obtained with a longer end time. The point when equilibrium is reached coincides with saturation in SCEPTIC's diagnostic for particle fluxes on the probe. This is not a big surprise, since the potential is calculated from this flux, but it proves that the saturation of the flux is a sufficient criterion for convergence of the solution. The equilibration time increases for larger domains. The reason for this

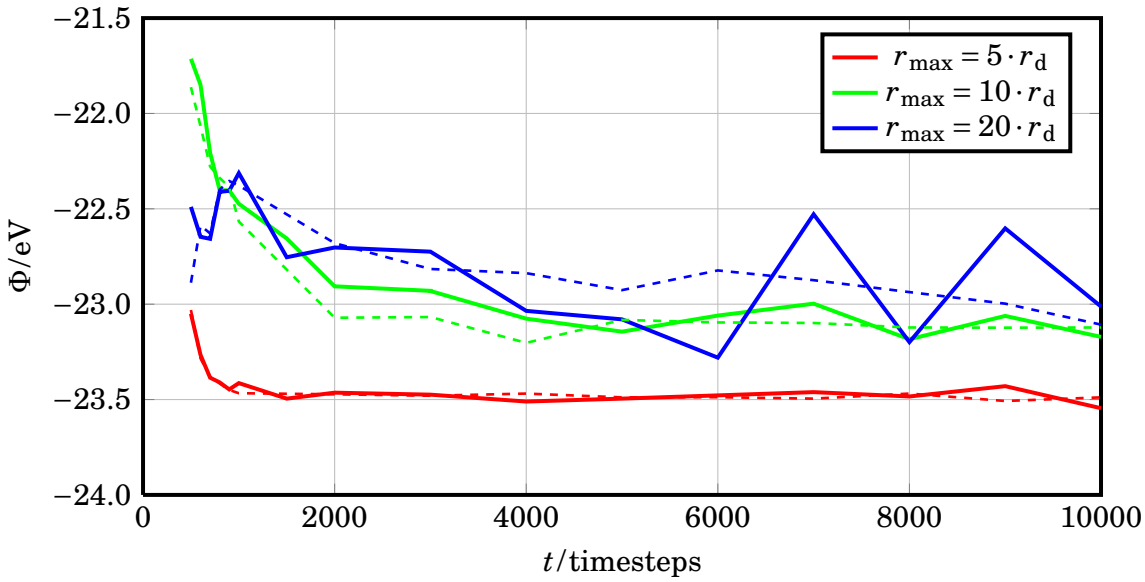

Fig. 5.6: Floating potentials of a dust grain with 3.2 µm radius in Hydrogen simulated with different domain sizes $r_{\max}$. Simulation was stopped after different times. Dashed lines refer to simulations with the fourfold number of particles.

is that particles injected at the outer boundary must travel for a longer time until they can get absorbed. This means that $n_{e,\infty}$ and Φ_d reach their terminal values more slowly.
Statistical fluctuations around the mean equilibrium value increase with domain size. This effect is linked to the statistical weight of the particles. The resolved domain area scales with $r_{\max}^2$. If one assumes a constant ion density, the number of real particles in the domain scales with this area. Because the number of particles is kept constant, the number of real particles per super particle scales with $r_{\max}^2$ as well. The influence of single particles increases. Ion densities close to the dust are higher than the ones in the (newly added) outer part of the domain, so the number of real ions in each super particle will grow a little slower than the area.
The dashed lines in figure 5.6 show the floating potential of similar runs with the fourfold number of particles (1600000 instead of the standard 400000). One can see, that variations in floating potential decrease strongly between these two series of runs. In fact, typical fluctuations within dashed lines are of comparable size with those of simulations with half the domain radius and four times less particles – which supports the explanation stated above.

5.2.2 Comparing P3M and SCEPTIC results

To supply SCEPTIC with parameters from P3M densities, temperatures and drift velocities are diagnosed within P3M at the locations of the dust. The ratio of temperatures and the ion drift velocity are used as input for SCEPTIC. The dust size was provided by calculating the electron Debye length from the P3M electron density and temperature and expressing it in units of the dust radius. Ions are injected by a shifted Maxwellian distribution. In this case $r_{\max} = 250 \cdot r_{\mathrm{d}}$ has been resolved using 25600000 particles.

With these input data SCEPTIC delivers potentials of -22.8 eV, -22.3 eV, -22.8 eV and -22.6 eV respectively. These values are very close i.e. independent of dust size, which complies with OML theory. The difference to potentials from P3M simulations is within 10 %, which is good compliance.
It is interesting, that both simulations give even more consistent results, when one looks at them separately. The potentials for different grain sizes are even closer than these 10 %. The reason for this is, that there are still small differences in simulated systems. For example, in P3M Maxwellian particles are initialized and accelerated in the sheath, where the dust is located. At this location there are already differences between electron and ion density large enough to have noticeable impact on the potential at which fluxes onto the grain compensate. SCEPTIC expects ion and electron density to be the same at its boundaries or at least at infinity. This is true for probes put into a plasma or dust in the bulk. If one does not assume $n_{\mathrm{e}} = n_{\mathrm{i}}$ in the equation used to determine the floating potential from the flux on page 24 a potential difference of

$$\Delta\Phi_{\mathrm{f}} = \frac{\mathrm{k_B} T_{\mathrm{e}}}{\mathrm{e}} \cdot \ln\left(\frac{n_{\mathrm{i}}}{n_{\mathrm{e}}}\right)$$

arises. This alone explains one fourth of the difference – even without considering the effects of a modified charge density calculation.

5.3 Dust in the Presheath of an Argon plasma

Laboratory plasmas are usually much colder than the Hydrogen plasma investigated above. They are also often heated by ccrf. While ions are too immobile to follow the fast oscillations of the field, electron velocity distributions change fast and are non-Maxwellian. This behaviour cannot be directly simulated with SCEPTIC, because Maxwellian electron velocities are assumed when estimating the floating potential. The reference parameters were obtained from the same code as used for the Hydrogen simulation in section 5.2. This time Argon was used instead of Hydrogen and instead using of a plasma source, the discharge was driven by a capacitively coupled RF heating. The plates where 5.2 cm away from one another and

n_i	$7.1 \cdot 10^8$	cm^{-3}
n_e	$7.1 \cdot 10^8$	cm^{-3}
T_i	0.025	eV
T_e	3.036	eV
$u_\mathrm{d,i}$	61.3	$\frac{\mathrm{m}}{\mathrm{s}}$
λ_Di	25	µm
λ_De	522	µm
ν_colls	$4.6 \cdot 10^6$	s^{-1}

Table 5.2: Plasma parameters of the P3M simulated Argon plasma at dust position.

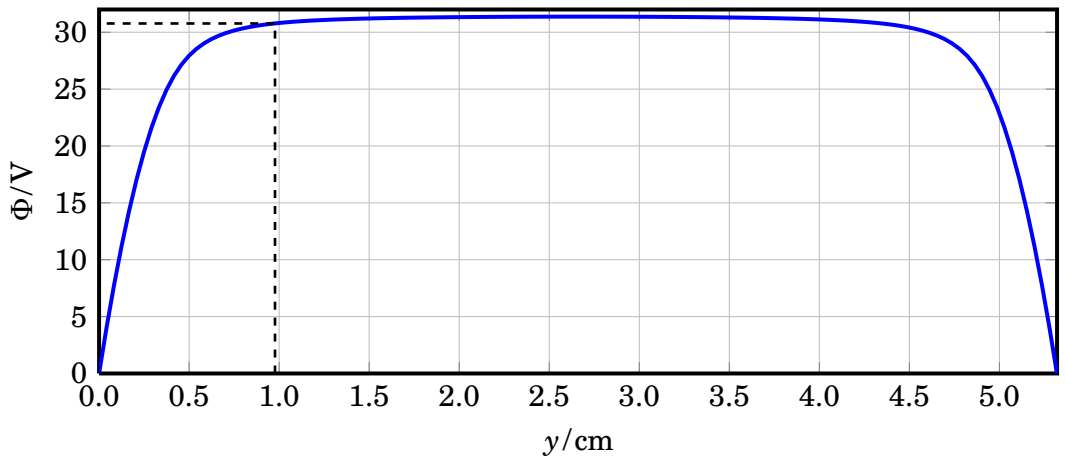

Fig. 5.7: Potential profile and dust position for the P3M simulatd Argon plasma.

driven with a voltage of 50 V at 13.56 Hz. These parameters resulted in a plasma as described in table 5.2. Densities, temperatures and velocities could be directly obtained from P3M output. They were averaged over 2000 rf periods and all cells in one plane perpendicular to the dust cell. The collision frequency was calculated by counting how often charge exchange collisions happen in this area and dividing this by the local ion density.

In subsequent P3M simulations grains with radii of 10 µm, 25 µm and 50 µm where immersed in the pre-sheath of that plasma. Their position, 9.8 mm from the left plate, is shown in figure 5.7. Their potentials were calculated to be $\Phi_\mathrm{d} = -3.79\,\mathrm{V}$, $\Phi_\mathrm{d} = -5.56\,\mathrm{V}$ and $\Phi_\mathrm{d} = -6.72\,\mathrm{V}$. This was done by diagnosing the electric field using

a specially designed finer grid in the MD region close the dust and integrating it from the unperturbed plasma to the dust position [25]. Contrary to the predictions of OML theory potentials are not independent of the grain size. The main reason for this is the high collisionality. The mean free path between charge exchange collisions is about 15 % of the Debye length.

5.3.1 Impact of changes in the collision frequency

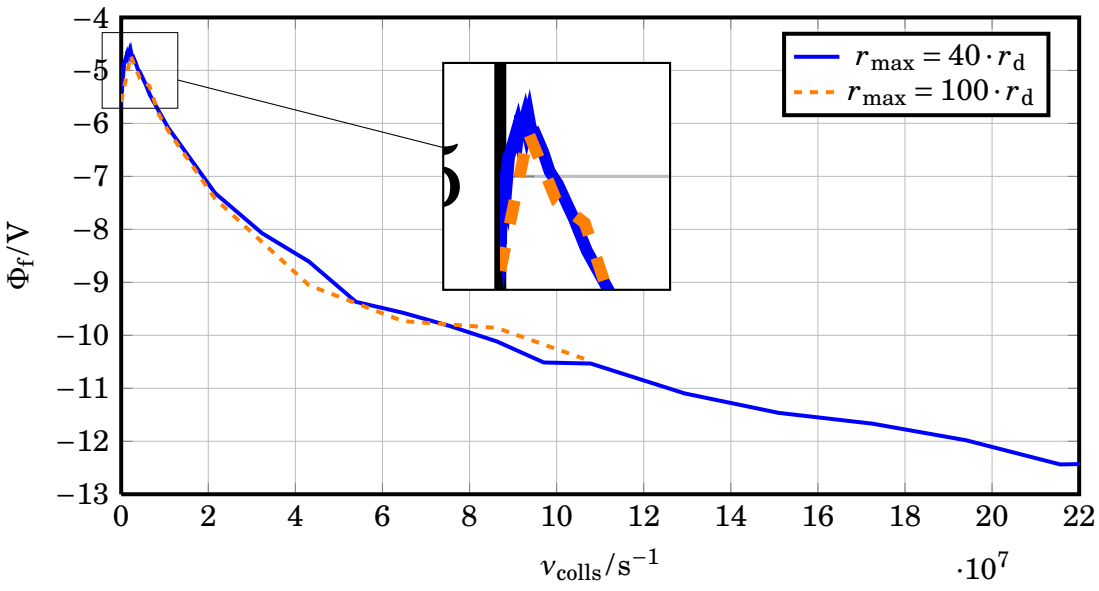

Fig. 5.8: 25 µm dust grain in an Argon plasma with varied frequencies of charge exchange collisions.

Collisions have a large impact on the charge collection of a dust grain. Ions that have been accelerated by the dust potential lose their momentum and the streaming velocity becomes unimportant (at least in non-flowing background gases).
To investigate this influence a 25 µm dust grain in an Argon plasma as described in section 5.3 has been simulated. The only parameter changed is the collision frequency, which was varied from $\nu_{colls} = 0 \ldots 10^7\,s^{-1}$. The result is shown in figure 5.8. The floating potential first increases with a larger number of collisions. This happens, because ions that would otherwise be outside the collection radius or that have velocities that would allow them to just flow past the grain are stopped and may get accelerated towards the dust. This increases the ion flux to the dust and therefore its floating potential.
Collisions also make ions lose the additional momentum they obtained from the potential drop around the dust, which decreases the ion flow velocity. This can lead to

r_d	10 µm	25 µm	50 µm
Φ_{P3M} / V	-3.2418	-5.8916	-6.2067
Φ_S / V	-4.6972	-5.4613	-6.3092
$\Phi_{S,E=0}$ / V	-4.6808	-5.5663	-6.3908
$\Phi_{S,v=0}$ / V	-4.7072	-5.5854	-6.3923

Table 5.3: Dust potentials for differently sized grains in an Argon plasma. Simulations were performed with P3M and three input parameter sets for SCEPTIC.

a decrease of the ion current to the dust and therefore increase the floating potential. That is why the floating potential decreases again after a certain collision rate is reached.
The second line in figure 5.8 shows the floating potentials of simulations with similar parameters, but doubled domain size. Both series approximately show the same values and behaviour. This means that the collection range is well enough resolved in both cases – even though the collection range should increase with collisions. A possible explaination is the decelerating effect of charge exchange collisions. It is rather unimportant from where particles start with their initial velocity. Sufficient resolution is especially important, when the results of SCEPTIC and P3M are compared.
Floating potentials vary by more than a factor of two within the range of simulated collection frequencies demonstrating their importance.

5.3.2 Comparing P3M and SCEPTIC results

SCEPTIC simulations have been performed with 25600000 particles, to ensure statistical reliability. The domain size was chosen to be $40 \cdot r_d$ for the two larger dust grains and $100 \cdot r_d$ for the smallest one. Using the ion velocity distribution from the P3M simulation in SCEPTIC did not make significant differences to SCEPTIC's velocity distribution. This can be explained by the high collisionality leading to a near Maxwellian ion velocity distribution. Because the latter uses an analytical approach, it has well resolved long tails and it allows for a better comparison with the standard code.
The simulations have been performed three times for every dust size: Once with all options activated, once without electric field and once without electric fields and drift velocity. Results are presented in table 5.3.
Potentials calculated with both codes are very close (2 % to 7 %) for the two larger grains. P3M calculated potentials for the 10 µm grain are about 30 % larger than

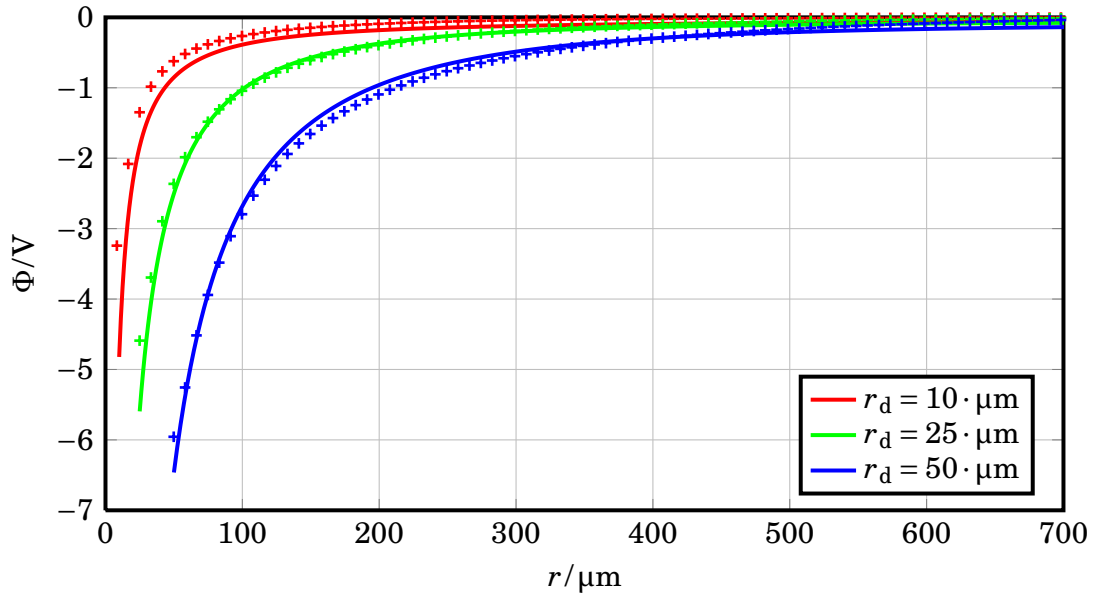

Fig. 5.9: Potentials near the probe for simulations of differently sized dust grains in an Argon plasma. Solid lines mean SCEPTIC results, crosses mean P3M results. Different colors indicate different dust sizes.

those generated by SCEPTIC – which is neither close nor very distant. One reason for the larger discrepancy for the smaller grain size might be charge fluctuations that arise from the discrete and stochastic nature of particle fluxes. It has been shown that dust charges Q vary with a root mean square of $\Delta Q_{\mathrm{rms}} \propto \sqrt{\langle Q \rangle}$ with N being the number of charges particles on a dust grain [33]. Because smaller particles collect fewer charges such fluctuations have higher impact on potentials calculated by both models.
One should also note, that only SCEPTIC directly calculates the floating potential. P3M instead counts the charges, that hit the dust. To retrieve a floating potential, the electric field is diagnosed and integrated on a sub grid in the MD region close to the dust. The floating potential is then obtained by averaging the potential at points closest to the dust surface. This may contain errors, because the steep potential gradients in this region amplify the effect of spatial deviations. Calculating the potential from the dust charge with a capacitor model as described by Whipple et al. [32] gives a wrong result, probably due to missing finite size effects. Since SCEPTIC can not explicitly calculate the number of absorbed electrons, but instead assumes perfect flux compensation at all times a comparison of dust charges is not possible.

5.3.3 Comparison of potentials around the probe

Figure 5.9 shows the potential drop near the three dust grains in Argon plasma which have been described in section 5.3.2. The plotted lines refer to the results of SCEPTIC simulations (with enabled electric field and drifting ions) while crosses mark results of P3M simulations. Potential distributions that have been generated in P3M only use potentials measured perpendicular to the RF direction while SCEPTIC's potentials are averaged over all angles. This does not introduce large errors, because high collisionality limits the effect of the flow velocity.
Potentials are very close at all distances for the two larger grains. Around the 10 µm grain P3M delivers a significantly higher potential than SCEPTIC does. A possible reason for this are finite size effects.

5.4 Synopsis

For this chapter dusty plasmas have been simulated with two codes that utilize very different approaches. SCEPTIC allowed to study the influence of ion temperatures and collisions without changing any other parameters. It was shown that lower ion temperatures result in a higher floating potential, because ions are collected from a larger region and that resolving this ion collection range is essential for obtaining reliable results. It was also shown that a small amount of collisions leads to the same effect as lowering the temperature while higher collisionalities slow down the ions that flow onto the dust – resulting in a decreased potential.
Results obtained from simulating the same systems with SCEPTIC and P3M agreed very well in both analyzed plasmas. This implies, that both codes deliver reliable results in fusion plasmas as well as in highly collisional low-temperature plasmas.

6 Summary

In this work complex plasmas, which was considered as plasmas with additional species beyond just electrons and one single ion species, have been studied with simulations. Using computational physics a better understanding of the underlying processes in such plasmas was obtained for two different cases.
In the first part of the thesis an experiment by Küllig et al. [10] was analysed using kinetic simulations. In the experiment the electron density of an Oxygen plasma was measured by microwave interferometry. A laser was adjusted such that both beams cross in a diagnostic volume. When the laser was switched on all negative ions along its beam emit electrons. From the temporal change of the integrated ion density measured using the interferometer the relaxation of the electron density was studied and the density of negative Oxygen ions was derived.
Simulations were performed using the Particle-in-Cell method. Virtual diagnostics for the detachment of electrons was added to an existing code written by Konstantin Matyash to self-consistently analyse the perturbation process. Like in experiment, electrons are detached from all negative ions in a diagnostic region in the bulk of plasmas with different electronegativities. The relaxation processes were studied by calculating the dynamics of particle densities and reaction rates in and near the detachment region. It was found that the dominating relaxation process is the creation of negative ions by dissociative attachment in agreement with the suggestions in the experemental paper. Nevertheless at higher electronegativities, the influence of transport processes get important. Decay times of the densities are influenced directly, by electrons leaving the detachment region, or indirectly, by adiabatic cooling of the electrons and therefore by impeding the dissociative attachment process. The simulated relaxation times are close to those measured for high electronegativities in the experiment. Very low electronegativities could not be modelled, because of the computational effort needed to overcome the statistical limits. Significantly longer decay times similar to the experiment appeared using an artificial detachment process, that increased the positive ion density, which mimicked strongly enhanced transport. This suggests that the reason for the much longer decay times observed experimentally in this regime is caused by changes in collisionality and therefore transport.

In the second part of the thesis dusty plasmas were simulated with two codes that use very different physics and numerics. The Particle-Particle Particle-Mesh code

by Konstantin Matyash models the whole plasma self-consistently. This gurantees correct results for plasmas, but is computationally extremely costly. Ian Hutchinson's code SCEPTIC treats only ions as kinetic particles. Electrons are assumed as background determined by the Boltzmann relation. Its floating potential is calculated from current balance using OML theory with Maxwellian electrons. This approximation, where electrons are not resolved kinetically and therefore charges on the dust are not calculated (only the dust potentials), was benchmarked against P3M. The impact of single parameters on the floating potential of a dust particle was studied. It was shown, that a small collision rate increases the ion flux to the probe and therefore lowers the floating potential, while the opposite is the case for highly collisional plasmas. It was also shown, that the floating potential increases for lower ion temperatures, because ions can be collected from a larger domain. Results from SCEPTIC and P3M have been compared for dust in a fusion plasma and in a highly collisional low-temperature plasma. They agreed very well in both cases, which implies, that their results are reliable in both regimes. For particles located in the sheath remaining differences between the codes can be explained by the fact that in this case the plasma is not quasi-neutral in the proximity of the dust particle, which is an assumption made by SCEPTIC.

Simulations presented within this thesis showed that kinetic modelling is a very helpful utility for the analysis of plasmas, allowing a better understanding of experiments. It was also demonstrated that comparison of different physics and numerics by benchmarking SCEPTIC with P3M supports the reliability of results from both codes. Computational physics is a fundamental and independent method as experimental and theoretical physics. A necessary prerequisite for successful work in this discipline is a close contact with experiment as well as with theory. In addition, the capability is needed to extract in a hierarchical approach simplified models from complex numerical models. Diagnostics of the complex numerical simulations allow to extract simpler models and to identify the basic principles of a specific problem for better understanding.

Bibliography

[1] E. R. Williams, S. G. Geotis, and A. B. Bhattacharya, "A radar study of the plasma and geometry of lightning," *J. Atmos. Sci.*, vol. 46, no. 9, pp. 1173–1185, 1989. doi: 10.1175/1520-0469(1989)046<1173:ARSOTP>2.0.CO;2.

[2] J. C. McLennan and G. M. Shrum, "On the origin of the auroral green line 5577 angstrom, and other spectra associated with the aurora borealis," *Proceedings of the Royal Society of London. Series A*, vol. 108, no. 747, pp. 501–512, 1925.

[3] A. Hewish and M. Symonds, "Radio investigation of the solar plasma," *Planetary and Space Science*, vol. 17, no. 3, pp. 313–320, 1969.

[4] C. K. Goertz, "Dusty plasmas in the solar system," *Rev. Geophys.*, vol. 27, no. 2, pp. 271–292, 1989.

[5] J. F. Waymouth and F. Bitter, "Analysis of the plasma of fluorescent lamps," *Journal of Applied Physics*, vol. 27, no. 2, pp. 122–131, 1956.

[6] J. P. Boeuf, "Plasma display panels: physics, recent developments and key issues," *Journal of Physics D: Applied Physics*, vol. 36, no. 6, p. R53, 2003.

[7] M. A. Lieberman and A. J. Lichtenberg, *Principles of Plasma Discharges and Materials Processing*. Wiley-Interscience, 2 ed., April 2005.

[8] M. Sekine, "Dielectric film etching in semiconductor device manufacturing: Development of sio2 etching and the next generation plasma reactor," *Applied Surface Science*, vol. 192, no. 1–4, pp. 270–298, 2002.

[9] L. Wegener, "Status of wendelstein 7-x construction," *Fusion Engineering and Design*, vol. 84, no. 2–6, pp. 106–112, 2009.

[10] C. Küllig, K. Dittmann, and J. Meichsner, "A novel approach for negative ion analysis using 160 GHz microwave interferometry and laser photodetachment in oxygen cc-rf plasmas," *Plasma Sources Science and Technology*, vol. 19, p. 065011, 2010.

[11] K. Matyash, "Kinetic modeling of multi-component edge plasmas,". PhD thesis, University Greifswald, Germany, 2003.

[12] I. Hutchinson, "Ion collection by a sphere in a flowing plasma: 3. floating potential and drag force," *Plasma physics and controlled fusion*, vol. 47, p. 71, 2005.

[13] A. Piel, *Plasma Physics*. Springer-Verlag Berlin Heidelberg, 2010.

[14] L. Lewerentz, "Surface effects in complex plasmas," Diploma thesis, University Greifswald, Germany, Aug. 2010.

[15] P. K. Shukla and A. A. Mamun, *Introduction to dusty plasma physics*. Institute of Physics Publishing, 2002.

[16] H. Mott-Smith and I. Langmuir, "The theory of collectors in gaseous discharges," *Phys. Rev.*, vol. 28, pp. 727–763, 1926.

[17] J. E. Allen, "Probe theory - the orbital motion approach," *Physica Scripta*, vol. 45, no. 5, p. 497, 1992.

[18] R. Hockney and J. Eastwood, "Computer simulation using particles," *McGraw-Hill, New York*, 1981.

[19] C. K. Birdsall and A. B. Langdon, *Plasma physics via computer simulation*. Institute of Physics Publishing, 1985.

[20] F. Bronold, K. Matyash, D. Tskhakaya, R. Schneider, and H. Fehske, "Radio-frequency discharges in oxygen: I. Particle-based modelling," *Journal of Physics D: Applied Physics*, vol. 40, p. 6583, 2007.

[21] D. Tskhakaya, K. Matyash, R. Schneider, and F. Taccogna, "The Particle-In-Cell Method," *Contributions to Plasma Physics*, vol. 47, no. 8-9, pp. 563–594, 2007.

[22] W. H. Press, S. A. Teukolsky, W. T. Vetterling, and B. P. Flannery, *Numerical Recipes in C*. Cambridge University Press, 1992.

[23] T. Takizuka and H. Abe, "A binary collision model for plasma simulation with a particle code," *J. Comp. Phys.*, vol. 25, pp. 205–219, 1977.

[24] N. Sydorenko, O. Grulke, K. Matyash, R. Schneider, S. Ullrich, and T. Klinger, "Negative ions in helicon oxygen discharges," *Contributions to Plasma Physics*, vol. 49, pp. 27–35, 2009.

[25] R. Ikkurthi, "Kinetic simulations of dusty plasmas,". PhD thesis, University Greifswald, Germany, 2009.

[26] K. Matyash, R. Schneider, F. Taccogna, and D. Tskhakaya, "Finite size effect of dust charging in the magnetized edge plasma," *Journal of Nuclear Materials*, vol. 363–365, pp. 458–461, 2007.

[27] K. Matyash, R. Schneider, R. Ikkurthi, L. Lewerentz, and A. Melzer, "P3m simulations of dusty plasmas," *Plasma Phys. Control. Fusion*, vol. 52 (12), p. 124016, 2010.

[28] I. Hutchinson, "Ion collection by a sphere in a flowing plasma: I. quasineutral," *Plasma physics and controlled fusion*, vol. 44, p. 1953, 2002.

[29] I. Hutchinson, "Ion collection by a sphere in a flowing plasma: 2. non-zero debye length," *Plasma physics and controlled fusion*, vol. 45, p. 1477, 2003.

[30] I. Hutchinson and L. Patacchini, "Computation of the effect of neutral collisions on ion current to a floating sphere in a stationary plasma," *Physics of plasmas*, vol. 14, p. 013505, 2007.

[31] M. Shibata, N. Nakano, and T. Makabe, "The effect of laser-induced photodetachment in O_2 rf discharges," *Journal of Physics D: Applied Physics*, vol. 30, p. 1219, 1997.

[32] E. C. Whipple, T. G. Northrop, and D. A. Mendis, "The electrostatics of a dusty plasma," *J. Geophys. Res.*, vol. 90, no. A8, pp. 7405–7413, 1985.

[33] C. Cui and J. Goree, "Fluctuations of the charge on a dust grain in a plasma," *IEEE Transactions on Plasma Science*, vol. 22, pp. 151–158, Apr. 1994.

Acknowledgements

At the very end of this work, I want to take the chance to express some words of gratitude to all the people, who helped me getting to this place. First of all I want to thank my advisor Ralf Schneider for his constant support and advice. The same gratitude belongs to Konstantin, for letting me use and modify his codes and for his patience when discussing about results. Both of them have also been a very great help in the critical last phase of writing this thesis.
Furthermore I want to thank the whole CompuS group for many small things and a pleasant work climate. I especially want to highlight Lars, who gave me answers to a lot of questions concerning details of Konstantin's code and an octave script collection, that helped me to get started with data analysis. Morten and Stefan often came up with little tricks that made it easier to move and process data.
Big thanks also go to Henry and Mathias, who kept the cluster alive most of the time and special thanks go to Ian H. Hutchinson for writing SCEPTIC, putting it online and allowing everybody on the world to use it.
Last not least I want to thank my family for their support and guidance throughout my life.